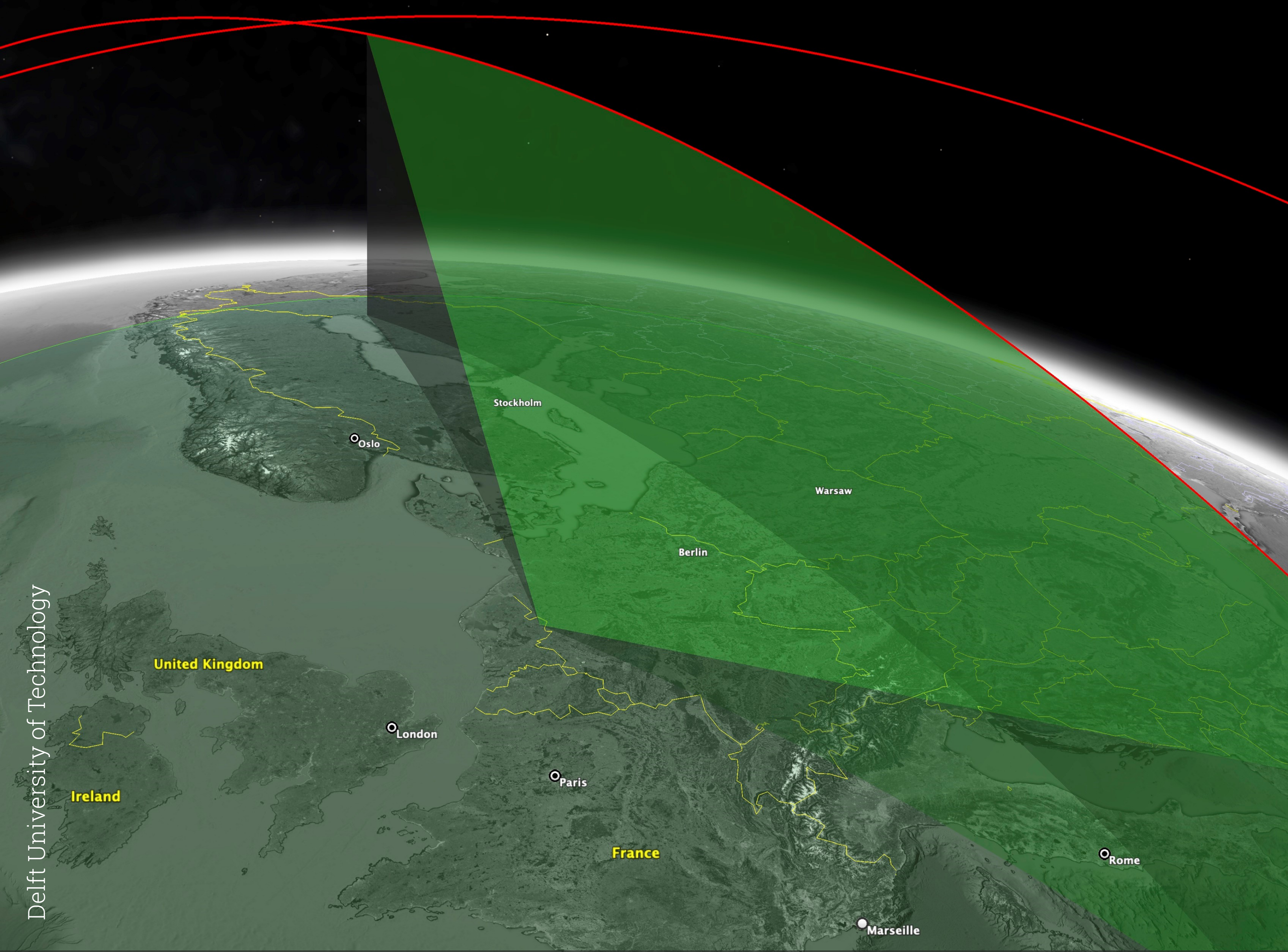

Delft University of Technology

Initial Orbit Determination using Long-Range Surveillance Radar

MSc Thesis

LTZ3(TD) N. (Niek) Schouten

TUDelft

THALES

Initial Orbit Determination using Long-Range Surveillance Radar

by

LTZ3(TD) N. (Niek) Schouten

to obtain the degree of Master of Science

at the Delft University of Technology,

to be defended publicly on Monday July 25, 2024 at 09:00 AM.

Student number:	4644514	
Project duration:	November 12, 2023 – July 25, 2024	
Thesis committee:	Dr. S. Gehly,	TU Delft, Supervisor
	Prof. Dr. Ir. P.N.A.M. Visser,	TU Delft, Chair
	Ir. B.T.C. Zandbergen,	TU Delft, Examiner
	Dr. Ir. E.P. van der Poel,	Thales, Supervisor

This thesis is confidential and cannot be made public until July 25, 2029.

An electronic version of this thesis is available at `http://repository.tudelft.nl/`.

TU Delft

Preface

This thesis marks the culmination of my research into the application and optimisation of radar-based tracking methods for space objects, undertaken as part of my Master's degree in Aerospace Engineering at TU Delft. Throughout this journey, I have delved deeply into the complexities of Initial Orbit Determination (IOD) algorithms and their efficacy in tracking non-cooperative space objects, a critical challenge in the context of increasing space activities and the growing threat of space debris. This research not only advances our understanding of radar tracking capabilities but also aims to contribute valuable insights towards enhancing the safety and sustainability of space operations.

I am profoundly grateful to my supervisors, Steve Gehly and Erwin van der Poel, for their support, insightful guidance, and feedback throughout this research process. Their expertise and encouragement have been instrumental in shaping the direction and depth of this study. I also extend my appreciation to Thales Nederland for their collaboration and for providing access to the radar data and technical resources necessary for this research.

Finally, I would like to acknowledge the enduring support and patience of my fiancée, family and friends. Their encouragement has been a constant source of motivation, particularly during the challenging phases of this project. This thesis is a testament not only to my academic and professional growth but also to the collective efforts and support of those who have been part of this journey. It is my hope that the findings and methodologies presented here will serve as a foundation for future advancements in space object tracking and contribute meaningfully to the field of aerospace engineering.

LTZ3(TD) N. (Niek) Schouten
Den Helder, July 2024

Abstract

This thesis addresses the issue of space debris tracking through the development and evaluation of advanced radar-based *Initial Orbit Determination* (IOD) algorithms and optimised measurement strategies. Space debris presents a challenge to space missions, necessitating tracking methods that do not require cooperation from the objects being tracked. The *batch least squares estimator* (BLSE), *extended Kalman filter* (EKF), *unscented Kalman filter* (UKF), and *unscented batch estimator* (UBE) were evaluated using both simulated and real radar data from the Sentinel-1A satellite. The UBE algorithm showed the lowest root-mean-square error (RMSE) and fastest convergence, effectively managing the non-linear complexities of orbit determination.

Four radar measurement strategies were examined to determine the minimum number of observations required for accurate orbit prediction and reacquisition. Strategies that provided full coverage and focused on the closest point of approach (CPA) demonstrated the most reliable results such as the inbound-CPA-outbound method and the changing radar update time. The study also investigated the impact of excluding specific radar measurements, such as range, radial velocity, azimuth, or elevation, on the accuracy of orbit estimation. It was found that a combination of range and angle measurements provided the most accurate results.

Contents

List of Figures

List of Tables

1

Introduction and Literature Review

With the advancement of aerospace technology, which has significantly reduced the barriers to satellite launch capabilities, Earth's orbit is experiencing an escalating congestion due to space debris. This issue has been escalating since the launch of Sputnik 1 in 1957, marking the start of the accumulation of human-made debris in space [1]. Over recent decades, space missions executed by organisations such as the *National Aeronautics and Space Administration* (NASA) and the *European Space Agency* (ESA), have contributed to a substantial accumulation of space debris in orbit [2]. This phenomenon not only presents a heightened risk of collision for operational satellites [3] but also poses a challenge to the long-term sustainability and accessibility of outer space.

Recent data from ESA indicates a critical situation in Earth's orbit, with approximately 36,500 pieces of space debris larger than 10 cm, about 1,000,000 objects measuring between 1 cm and 10 cm, and in excess of 130 million objects ranging in size from 1 mm to 1 cm [4]. This proliferation of orbital debris presents a substantial risk to the future of space exploration and utilisation. The escalating density of objects in orbit proportionally increases the likelihood of collisions, posing significant hazards to operational satellites, forthcoming space missions, and the safety of astronauts aboard space stations. Additionally, these *resident space objects* (RSOs) adversely impacts astronomical research, as observations are increasingly obstructed by these remnants [5].

On February 10, 2009, a major incident occurred: the collision of two communication satellites, Iridium 33 and Kosmos 2251, at a velocity of 11.7 km/s. Post-collision, the *U.S. Space Surveillance Network* (SSN) detected over 2300 traceable fragments of space debris, indicating the complete destruction of both satellites [6, 7]. This event exemplifies the scenario hypothesised by Donald J. Kessler in 1978, where an increase in satellite numbers elevates collision probabilities, potentially leading to a cascading effect of debris accumulation around Earth [8].

The collision between Iridium 33 and Kosmos 2251 underscores the complexities and risks associated with Earth's orbit, emphasising the need for effective space debris management and the critical role of orbit determination and prediction. The history of astrodynamics, which encompasses the study of the motion of astronomical objects, has been shaped by contributions from renowned physicists and mathematicians since Johannes Kepler first formulated the laws of planetary motion in 1609 [9]. Notably, Kepler's Rudolphine Tables in 1627 [10] enabled accurate predictions of celestial events, while Isaac Newton, Johann Heinrich Lambert, and Carl Friedrich Gauss further advanced the field through significant theoretical and practical advancements. Lambert's theorem for orbit determination using two position vectors and elapsed time [11], mathematically validated by Joseph-Louis Lagrange [12], and Gauss's method for using three pairs of angles [13] are seminal works that have laid the foundation for modern astrodynamics. This field, once focused on celestial bodies like moons, planets, and asteroids, has evolved to include artificial satellites, with pioneers such as Leonhard Euler, Pierre-Simon de Laplace, and again, Gauss and Lagrange, contributing to its development through methods that are still relevant for addressing contemporary astrodynamical problems [14].

The methods introduced by Lambert, Laplace and Gauss are considered to be the classical deterministic *initial orbit determination* (IOD) algorithms, while modern adaptations have incorporated computer algorithms, such as the double-r iteration method introduced by Escobal [15], and Gooding's method [16]. These methods have a deterministic approach, in the sense that six observations are used to solve for six orbital elements. However, the reality of spacecraft orbits influenced by various perturbing forces and measurement inaccuracies, necessitated a shift towards a statistical approach for IOD in the 1960s. From the start of the space race, countries have been launching human made satellites into orbit, many of which were intended for scientific purposes and thus required precise orbit determination solutions.

Over the years, many algorithms have been developed, but to know which algorithm would be best, it must be applicable to the type of observation data and the number of observations. Here, a distinction is made between long arc (dense data) and short arc (sparse data). Long arc data refers to tracked satellite observations, which can have up to a hundred observations within a full pass over the sensor. On the other hand, short arc data refers to satellite observations such as photographs with satellites streaks or radar observations in a certain sector, where observations are made typically over a few seconds.

1.1. Long arc (dense data)

For long arc data, two primary algorithm types can be distinguished, namely batch estimation and sequential filtering. Batch estimation processes all data over a fixed period together and is commonly employed in non-near-real-time applications like precise orbit determination [17]. Sequential filtering, on the other hand, is preferred for applications like on-board satellite navigation that require near-real-time data processing.

The most recognised batch estimation technique is the *batch least squares estimator* (BLSE), which was first proposed by Gauss in 1809 [13]. Traditionally, this method aims to minimise the sum of the squares of the calculated observation residuals. However, it is important to note that the standard least squares algorithm treats all measurements as equally important. In many applications, users opt for a more refined approach, such as the *weighted least squares* or the *minimum variance least squares*, which accounts for the expected measurements noise characteristics to produce the minimum variance estimate. The minimum variance least squares is commonly assumed to be the normal least squares method and takes the covariance matrix of the observations into account.

The first sequential filter, introduced by Rudolf Kalman, was the *Kalman filter* (KF) [17]. This filter provides an efficient recursive solution to the least squares problem and is adaptable for use with dynamical noise models. The Kalman filter, though developed for linear problems, necessitated adaptations for the highly nonlinear nature of orbit determination. A few of these adaptations are the Square root Kalman filter [18], central difference Kalman filter [19], ensemble Kalman filter [20], Schmidt-Kalman filter [21], Invariant Extended Kalman filter [22] and, Monte Carlo Kalman filter [23]. The *extended Kalman filter* (EKF) [24, 25] is a popular derivative of the Kalman filter. The extended Kalman filter linearises the equations of motion and measurement equations around the most recent estimate, applying the Kalman filter update equations to the linearised system. However, its simplifying linearisation assumption can fail in highly nonlinear problems, leading to inaccurate estimates [26–28].

The *unscented Kalman filter* (UKF) [29, 30], based on the unscented transformation, avoids the linearisation process inherent in the EKF. It uses carefully selected sample points propagated with true nonlinear dynamics, resulting in higher consistency compared to the EKF [27]. The unscented transformation is founded on the intuition that *"it is easier to approximate a probability distribution than it is to approximate an arbitrary nonlinear function or transformation"* [29]. The UKF has been extensively investigated for its use with various dynamics systems, including determining a satellite attitude [31], or its orbit [32, 33] or the trajectory of ballistic missiles [34]. This research has demonstrated the superior performance of the unscented Kalman filter in highly nonlinear situations.

Although the batch least squares estimation and the extended Kalman filter are the most widely used for solving nonlinear parameter estimation problems [17, 31, 35–37], they have some flaws due to the linearisation process. Typically, both methods are applied to nonlinear systems by linearising and approximating all the nonlinear models. For orbit determination, the dynamic system is linearised about the reference trajectory with the assumption that the reference trajectory is very close to the true trajectory. This linearisation in the batch least squares estimation and the extended Kalman filter may cause a large error, instability, and divergence in the estimation process when the initial reference trajectory condition is not accurate, and the measurement data are sparse or insufficient [33]. Because of the good performance of the UKF, and without the inherent drawbacks of linearization techniques, Park et al. [38] were motivated to research a non-recursive batch estimator without linearisation and using the unscented transformation, which could be interpreted as an *unscented batch estimator* (UBE).

The particle filter (PF) [39], another type of sequential filter, is employed for non-Gaussian distributions. This filter is particularly useful in nonlinear models where the actual distribution of position and velocity is non-Gaussian. The particle filter, as a sequential Bayesian algorithm, estimates the required state probability density function using a set of random samples (particles) with corresponding weights [40–42].

1.2. Short arc (sparse data)

For short arc observations, the classic IOD algorithms and their modern interpretations remain in use. However, Milani et al. introduced a new technique known as the admissible region [43]. The technique was intended for celestial object tracking using a single observational arc. Tommei et al. introduced it to the case of angles-only initial orbit determination for space debris [44], where azimuth and elevation measurements are done using optical sensors. The admissible region is defined as the set of physically acceptable orbits, for example orbits with negative energy (as they are non-escape orbit). Given additional constraints on the semi-major axis, eccentricity, etc., the admissible region is further constrained, resulting in the constrained admissible region (CAR). Based on known statistics of the measurement process, the hard constraints are replaced by a probabilistic representation, known as the probabilistic admissible region (PAR) [45]. The Possibilistic Admissible Region (PAR+), derived from the outer probability measure (OPM), represents an alternative to probability theory for uncertainty representation [46]. Moreover, the admissible region has been widely studied for the tracklet association problem [47–50]. DeMars and Jah approximated the admissible region by the Gaussian Mixture Model [51].

Expanding on the topic of tracklet association, Siminski et al. [8,9] grouped methods involving the *initial value problem* (IVP) and *boundary value problem*(BVP). These approaches reformulate tracklet association as an optimisation process for optical measurements, employing two distinct loss functions and optimisation techniques. Their application was demonstrated using tracklets from objects in the *geostationary Earth orbit (GEO)*. Both methods necessitate calibration for measurement noise. The BVP method, leveraging range hypotheses and a Lambert solver, exhibits superior robustness and efficiency in hypothesising orbital states. Conversely, the IVP approach, while independent of the Lambert solver and more straightforward, is susceptible to inaccuracies from incorrect noise model assumptions, potentially leading to sub-optimal association performance. Additionally, the IVP loss function's valleys are challenging to segregate, complicating the optimisation process and escalating computational demands due to the need for numerous initial points.

1.3. Algorithm selection

Today, advanced methods like the *Global Navigation Satellite System (GNSS)* and *satellite laser ranging (SLR)* are used in orbit determination. These methods have proven to be very accurate, yet they require a specific configuration and cooperation. For GNSS, the satellite requires onboard transmitters and receivers, whereas SLR needs satellites equipped with retro-reflectors [37]. However, their applicability to space debris is limited due to potential damages to the satellite or uncontrolled spins. This limitation has led to the use of alternative methods such as *electro-optical (EO)* systems (including telescopes), and radar. Despite their long standing use, EO systems are hindered by environmental constraints, such as poor weather or daylight interference.

In contrast, radar systems are versatile, functioning effectively under various weather conditions. Advancements in radar technology, like waveform design and increased power and antenna size, have made them suitable for detecting satellites in *Low Earth Orbit (LEO)*. Thales Nederland is a company that specialises in military radars and has a radar in their portfolio with this capability, which is the SMART-L MM. This is currently one of the largest L-band phased array radars. With this, they contribute to a significant increase in air surveillance and extended capabilities such as ballistic missile detection and space domain awareness [52]. The *active electronically scanned array (AESA)* technology enables the multi-mission features of this radar. With their cooperation, this study is set up.

The SMART-L MM radar can detect and track space objects. A track will result in roughly 100 measurements, hence long arc algorithms will be the focus for this research. In Figure 1.1, a roadmap of these algorithms can be seen, where the highlighted blocks indicate the selected algorithms for this study.

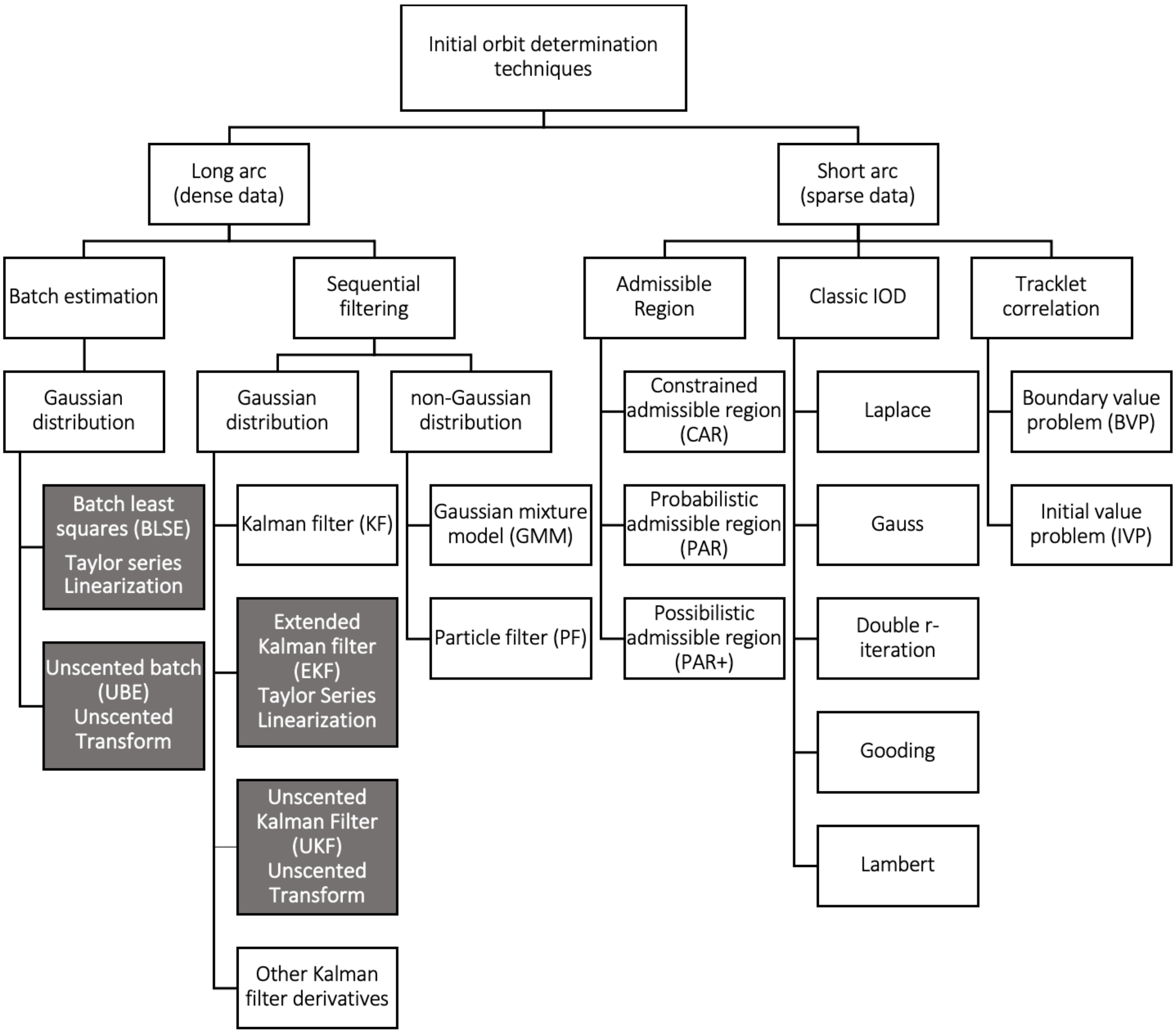

Figure 1.1: Road map of the developed initial orbit determination algorithms, the highlighted techniques are tested in this study.

To ensure a comprehensive and fair evaluation of the relative performances of these algorithms, it is essential to include both sequential and batch processing techniques in the study. Additionally, an intriguing aspect of this research is to investigate whether algorithms predicated on the Taylor series linearization exhibit any performance disparities compared to those based on the unscented transform. Consequently, for batch estimators, both the batch least squares estimator and the unscented batch estimator have been selected for thorough testing. Similarly, in the realm of sequential filters, the extended Kalman filter and the unscented Kalman filter will be examined.

By examining and comparing these four algorithms, the study aims to provide a comprehensive and representative overview of their functionalities and efficiencies in the context of long arc data processing for space object tracking. This analysis is anticipated to yield valuable insights into the strengths, limitations, and optimal application scenarios of each algorithm, thereby contributing significantly to the field of space situational awareness using radar.

The primary objective of this study is to create an overview of the performance of different IOD algorithms. The first research question is,

1: *Which IOD algorithm shows the lowest RMSE with radar data?*

Similar studies in this field take the *root mean square error (RMSE)* of the position and velocity, represented in Cartesian (x, y, z) or in the *local-vertical local-horizontal* (LVLH) (radial, along-track, cross-track) frames, as a performance measure [53–57]. The RMSE quantifies the deviation between the true orbit and the estimated orbit. Another measure that is often used, is the difference in position as a function of time. Once the best algorithm is found, the limits of this filter must be established. The first question arises from an operational perspective, aiming to optimise the radar budget, which refers to the allocation of radar resources and time. As previously mentioned, the SMART-L MM radar is designed for various missions, so it cannot be exclusively dedicated to tracking space objects. In practice, the radar is likely to be used predominantly for air surveillance, allocating only a small portion of its time to space situational awareness, resulting in a low radar time budget. Hence, the following question arises,

2: *What is the minimum number of radar measurements required to predict the orbit of an object accurately enough to reacquire it on the next orbital pass?*

And the final question is,

3: *How does the removal of specific radar measurements (range, range-rate, azimuth angle or elevation angle) impact the accuracy of the selected IOD algorithm?*

To answer the research questions, the following research structure is applied. First the theoretical foundations for orbit determination and radar physics is explained in chapter 2. Subsequently the methodology for the radar models and the orbit models is highlighted in chapter 3. Next, the results are discussed in chapter 4. Finally, the conclusion and recommendations are discussed in chapter 5. It is assumed that the reader is familiar with astrodynamics, calculus and statistics.

2
Theoretical Foundations

In this chapter, the relevant theory to support this study on initial orbit determination using long-range surveillance radar is presented. First, the fundamentals of radar theory is explained in section 2.1. Subsequently, orbital dynamics is explained in section 2.2, and finally the estimation techniques are explained in section 2.3.

2.1. Radar Measurements and Physics

In the theoretical framework of radar systems, special emphasis is placed on Pulse Doppler Radar technology, which contrasts with continuous wave (CW) radars by transmitting discrete bursts of electromagnetic energy. Radar fundamentally acts as an electromagnetic sensor, tasked with the detection and localisation of objects that reflect its signals. The principal operations of a radar system involve the emission of electromagnetic energy, which propagates through space, is reflected by targets, and is reradiated in various directions. A portion of this reradiated energy, or echo, is captured by the radar's antenna. Subsequently, the radar utilises internal amplification and signal processing to estimate the location of the target, alongside other potential information.

The information that can be derived about a target includes its range, calculated by measuring the time necessary for the radar signal to travel to the target and return at the speed of light; the radial velocity, determined through the Doppler frequency shift between the transmitted and received signals; the angular direction, identified by pinpointing the angle at which the echo signal's magnitude from a scanning array is maximal; and the signal-to-noise ratio (SNR). The SNR, vital for the accuracy of radar measurements and the detection of targets, depends on the ratio of the processed signal's total energy to the receiver's noise power per unit bandwidth.

Radar systems like the SMART-L MM use Pulse-Doppler radar technology, which takes advantage of pulse transmissions and Doppler information to calculate radial velocities. These radars feature a coherent train of pulses, ensuring a consistent phase relationship across successive RF pulses. This coherence concentrates the pulse train's energy spectrum around distinct spectral lines, determined by the pulse repetition frequency (PRF), aiding in the discrimination of Doppler shifts.

2.1.1. Physics of Electromagnetic Waves

Radar systems operate by transmitting and receiving electromagnetic (EM) pulses. An electromagnetic wave, which constitutes such a pulse, consists of electric ($\vec{E}$) and magnetic ($\vec{B}$) fields oscillating at the carrier frequency. The electric field oscillates in one plane, while the magnetic field is perpendicular to it. These waves travel at the speed of light (c), moving orthogonal to the plane formed by the $\vec{E}$ and $\vec{B}$ fields, as per the right-hand rule [58]. A depiction of an EM wave is provided in Figure 2.1.

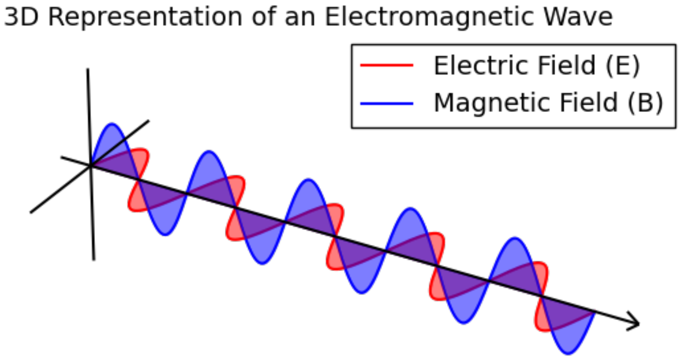

Figure 2.1: 3D visualisation of an EM wave. The electric field $\vec{E}$ is shown in red, the magnetic field $\vec{B}$ in blue, and the arrow indicates the direction of wave propagation.

The amplitude of the electric field can be expressed by the equation:

$$E = E_0 \cos(kz - \omega t + \varphi) \tag{2.1}$$

Here, E_0 is the peak amplitude, and φ represents the initial phase. The wave number k and the angular frequency ω are related as follows:

$$k = \frac{2\pi}{\lambda}, \quad \omega = 2\pi f \tag{2.2}$$

where λ is the wavelength, and f is the carrier frequency. The wavelength is the distance between two consecutive peaks or troughs, while the period T_0 denotes the time taken for one complete cycle. The frequency, defined as the inverse of the period, indicates how many cycles occur per second:

$$f = \frac{1}{T_0} \tag{2.3}$$

Given that EM waves travel at the speed of light, the product of wavelength and frequency equals c:

$$\lambda f = c \tag{2.4}$$

EM waves vary in type and function, from radio waves used in telegraphy to gamma rays in astrophysics, differentiated by their frequency. Radar systems typically operate within the 300 MHz to 35 GHz range.

2.1.2. Pulsed Waveform

Pulse radar emits EM waves for a brief duration, known as the pulse width τ. During emission, the receiver is disconnected or *blanked* from the antenna to shield its sensitive components from the transmitter's high-power EM waves. Consequently, no signal can be detected during this period, creating a blind range. The total time, comprising both the listening duration and the pulse width, is termed the *pulse repetition time* (PRT) or *pulse repetition interval* (PRI), illustrated in Figure 2.2.

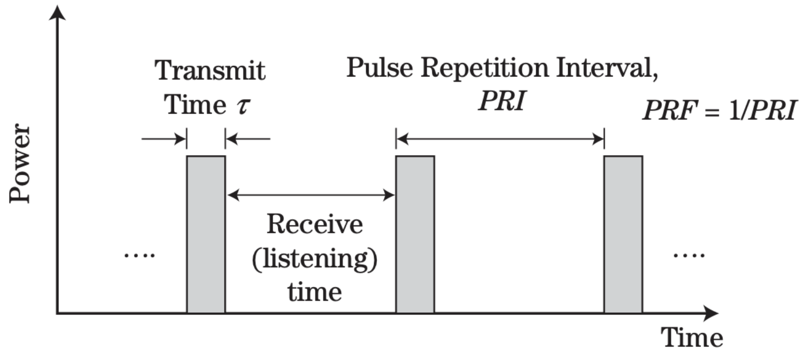

Figure 2.2: Illustration of a pulsed radar waveform, where the tall rectangles signify the transmitted pulses. [58]

The *pulse repetition frequency* (PRF) defines the number of transmit/receive cycles completed by the radar per second, calculated as:

$$PRF = \frac{1}{PRI} \tag{2.5}$$

The transmit duty cycle, DC, represents the fraction of time the transmitter is active during one radar cycle. It is calculated by:

$$DC = \frac{\tau}{PRI} = \tau \cdot PRF \tag{2.6}$$

Pulsed radar systems encounter specific challenges. The delay time between the transmission of a pulse and the reception of its reflection is used to determine the distance to a target. However, if the round-trip travel time of the pulse exceeds the PRT, it introduces a timing ambiguity and, consequently, a range ambiguity. This means the received pulse might be from the most recent transmission, indicating a nearby target, or it could be from a previous pulse, indicating a more distant target. This dilemma is depicted in Figure 2.3.

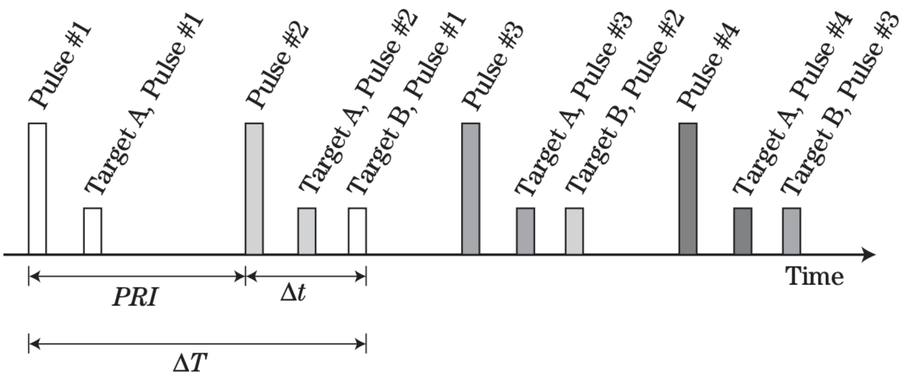

Figure 2.3: Demonstration of range ambiguity in a pulsed radar. Tall rectangles show transmitted pulses, and short rectangles show received echoes from two targets, with shading indicating the originating pulse. [58].

By choosing an appropriate PRI, range ambiguities can be minimised. The formula for the maximum unambiguous range is:

$$R_{ua} = \frac{c \cdot PRI}{2} \tag{2.7}$$

where c is the speed of light. This approach ensures the radar system can accurately interpret distances to targets without confusion from overlapping signals.

2.1.3. The Radar Equation

The radar equation establishes a relationship between a radar's range and various characteristics, including the transmitter, receiver, antenna, target, and the environment [59]. This equation, detailed in Appendix C, is expressed as follows [60]:

$$SNR = \frac{P_t \tau G_t A_e \left(RCS\right)}{\left(4\pi\right)^2 k T_s R^4 L_i} \tag{2.8}$$

Here, R denotes the range, P_t represents the transmit power, G_t is the gain of the transmitting antenna, τ refers to the width of the rectangular pulse, A_e stands for the effective aperture, and RCS indicates the radar cross-section of the target. The constant k is Boltzmann's constant (1.38×10^{-23} watt-second per Kelvin), T_s is the system noise temperature, SNR is the signal-to-noise ratio, and L_i encompasses the RF system losses. Many of these parameters are contingent on the radar's design and operational settings. For simplicity and for certain conditions, these variables can be incorporated into a constant, C, referred to as the radar budget. This consolidation leads to a more concise equation:

$$SNR = C \frac{RCS}{R^4} \tag{2.9}$$

2.1.4. Target Detection

In modern radar systems, the detection of targets is automated within the signal or data processor. This process typically involves setting a threshold signal level based on the prevailing interference, which includes noise and clutter. When the received signal surpasses this threshold, the presence of a target is indicated. An example of this mechanism is depicted in Figure 2.4, where a target declaration would occur at bin 50. However, such detection might not always indicate an actual target; it could also result from a significant noise spike, leading to a *false alarm*.

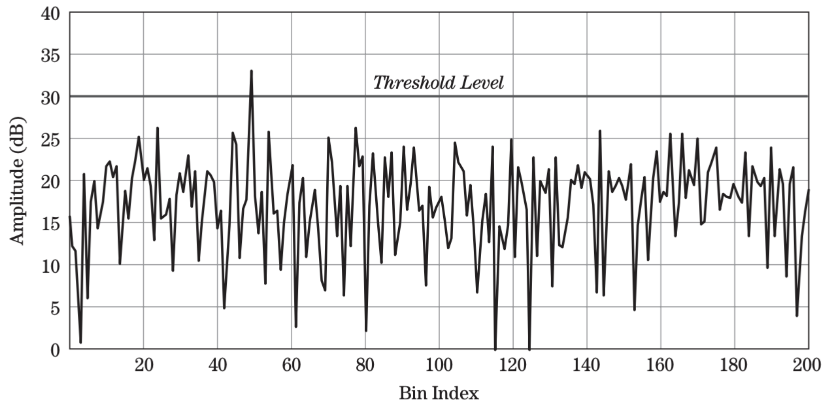

Figure 2.4: Illustration of threshold detection concept, highlighting a potential target detection at bin 50 [58].

The characteristics of the received signal are subject to variations in the target's radar cross-section (RCS), systemic losses and noise, and propagation effects attributable to the Earth's surface and atmosphere. Consequently, the detection process, which relies on signal voltage, is inherently statistical, characterised by a detection probability (P_d) and a probability of false alarms (P_{fa}).

2.1.5. Radar Cross Section and Swerling Cases

The most important property of the radar target is its *radar cross section* (RCS) [61]. This measure for the amount of reflected electromagnetic (EM) energy in the direction and at the location of the receiving antenna is indicated in effective reflected area:

$$RCS = 4\pi \frac{P_s}{S_i} \tag{2.10}$$

where, P_s is the scattered power in a specific direction and S_i is the energy density of the received echo. The RCS mainly depends on the shape, size, electromagnetic properties as well as the frequency of the pulse, aspect angle and the polarisation of the wave. Determining the RCS of real operational targets such as fighters, ships or in this case satellites, is very difficult, for both theoretical computer models and real RCS-measurements. With real measurements, due to vibrations, change in aspect angle and a change in the transmitted frequency (Frequency agility), you get time dependant RCS fluctuations. Peter Swerling studied these RCS fluctuations extensively in the 1950s, and he introduced statistical fluctuation models, currently known as Swerling cases [62]. Skolnik et al. described the Swerling cases as follows [59]:

The first case, *SW0*, assumes a target with a constant RCS without fluctuations. An example of a SW0 case, would be a smooth metal sphere offering uniform reflections, such as the *Lincoln Calibration Sphere 1* (LCS-1).

The second case, *SW1*, assumes a target composed of numerous similar reflectors, where the RCS changes slowly over time. An example of such a target would be a commercial airliner in steady flight. It components such as wings, fuselage and engines contribute to a stable overall RCS.

The third case, *SW2*, assumes a similar target as SW1, however, here the RCS changes rapidly over time. An example of a SW2 target would be an aircraft performing an evasive manoeuvre. Because of the changes in aspect angle, the RCS fluctuates rapidly over time.

The fourth case, *SW3*, assumes a target with one large reflector and multiple smaller reflectors, where the RCS changes slowly over time. An example of such a target would be a large ship with a dominating superstructure and additional smaller reflectors such as masts.

The final case, *SW4*, assumes a similar target as SW3, however, here the RCS changes rapidly over time. An example of this would be a missile, with a large reflective body and smaller stabilisation fins, doing a manoeuvre.

2.1.6. Error Sources

A radar is a very complex system. It consists of many subsystems, which are all prone to errors. The accuracy of the radar chain depends on the atmosphere, signal processing techniques, analogue-to-digital conversions, thermal noise in the cables, alignment and calibration of the system, the target and many more factors. In this subsection the noise error, glint error and instrument error are explored. Although the propagation error is a very interesting and relevant error source, the complexity of this subject is outside the scope of this study. Hence it is assumed that the radar's measurements are corrected for atmospheric and ionospheric refraction.

Noise error

Noise is the fundamental limitation of accurate radar measurements. Skolnik derived equations for theoretical accuracies of radar measurements on the assumptions that large signal-to-noise ratios are required for detection, detection must occur before meaningful information can be extracted about a target echo and that the measurement error associated with a particular parameter, is independent of the errors in any other parameter. He also assumed that the accuracy is only limited by received noise, and that all bias errors are accounted for [59].

The error in range depends on the error in time-delay accuracy. This relationship is as follows:

$$\delta_{R,n} = \frac{c}{2}\delta_{T_R,n} \tag{2.11}$$

The time of a pulse is based on locating the leading edge of the pulse and when it overrides a threshold. With noise added onto the signal, the position of the leading edge changes, inducing an error as seen in Figure 2.5. The error is proportional to the slope of the pulse or the rise time t_r. If the slope is steep, the error decreases. The rise time in turn, depends on the bandwidth of the pulse.

$$B \approx \frac{1}{t_r} \tag{2.12}$$

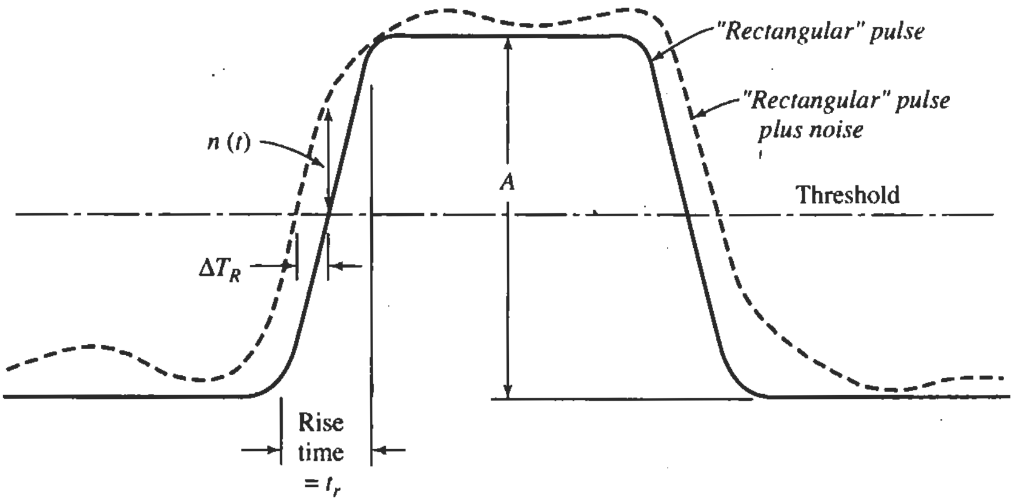

Figure 2.5: Measurement of time delay using the leading edge of the radar pulse. The solid curve is the echo of the pulse without noise. The dashed curve is the echo of the pulse with noise [59]

For a sinc function, this time delay is:

$$\delta_{T_R,n} = \frac{\sqrt{3}}{\pi B\sqrt{2SNR}} \tag{2.13}$$

Substituting Equation 2.13 into Equation 2.11, yields the range error:

$$\delta_{R,n} = \frac{c\sqrt{3}}{2\pi B\sqrt{2SNR}} \tag{2.14}$$

The accuracy in radial velocity depends on the error in frequency. The relationship between these two quantities is as follows:

$$\delta_{V_r,n} = \frac{\lambda}{2}\delta_{f_d,n} \tag{2.15}$$

Using the method of inverse probability, Manasse [63] showed that for a rectangular pulse, the error in frequency is:

$$\delta_{f_d,n} = \frac{\sqrt{3}}{\pi\tau\sqrt{2SNR}} \tag{2.16}$$

Hence, the error in radial velocity yields:

$$\delta_{V_r,n} = \frac{\lambda\sqrt{3}}{2\pi\tau\sqrt{2SNR}} \tag{2.17}$$

Finally, the angular measurements depend on the size of the aperture. The SMART-L MM radar, has a rectangular aperture with a height H and a width W. The errors in azimuth and elevation are:

$$\delta_{\phi,n} = \frac{\lambda\sqrt{3}}{\pi W\sqrt{2SNR}} \tag{2.18}$$

$$\delta_{\theta,n} = \frac{\lambda\sqrt{3}}{\pi H\sqrt{2SNR}} \tag{2.19}$$

These errors however, are not the standard deviation of the measurement. To calculate the standard deviation, the error has to be divided by the square root of the number of measurements m [64]. For radar, the number of measurements is 4.

$$\sigma_{R,n} = \frac{\delta_{R,n}}{\sqrt{m}} = \frac{\delta_{R,n}}{2} \tag{2.20}$$

In summary, the theoretical standard deviations caused by thermal noise in the radar system are:

$$\begin{bmatrix} \sigma_{R,n} \\ \sigma_{\phi,n} \\ \sigma_{\theta,n} \\ \sigma_{V_r,n} \end{bmatrix} = \begin{bmatrix} \frac{c\sqrt{3}}{4\pi B\sqrt{2SNR}} \\ \frac{\lambda\sqrt{3}}{2\pi W\sqrt{2SNR}} \\ \frac{\lambda\sqrt{3}}{2\pi H\sqrt{2SNR}} \\ \frac{\lambda\sqrt{3}}{4\pi \tau\sqrt{2SNR}} \end{bmatrix} \tag{2.21}$$

Glint error

Glint error occurs with complex and sizeable targets, where the target size is significant relative to the radar's wavelength, leading to multiple scattering centres within the radar's resolution cell. This phenomenon results in a temporal shift in the apparent location of the target compared to its reference point, often chosen as the target's centre of gravity [59, 65]. The scattering centre's movement across the target's geometry can lead to radar pointing discrepancies that exceed the target's actual physical dimensions, introducing measurement uncertainties [66]. Similar to the fluctuations observed in RCS, the variations in position and Doppler frequency stem from changes in aspect angles and wavelengths. Consequently, these fluctuations are statistically modelled to account for their unpredictable nature [67].

Barton [66] studied this phenomenon and found out that it is a rather complex statistical question, however, he derived three equations that can be used to approximate the glint error,

$$\sigma_{R,g} = \frac{L}{3} \tag{2.22}$$

$$\sigma_{ang,g} = \frac{L}{3R} \tag{2.23}$$

$$\sigma_{V_r,g} = \frac{\omega L}{3} \tag{2.24}$$

To give an indication of the numeric values of the glint error, consider the *International Space Station* (ISS). The ISS flies at an altitude ranging from 370 kilometres to 460 kilometres, and has a span of 109 meters [68]. Assuming an altitude of 370 km, at zenith, the glint error in range is roughly 36 meters and in azimuth and elevation, this is roughly 0.0056 degrees. Assuming that the ISS does not manoeuvre and flies overhead, the aspect angle changes roughly 180 degrees in 5 minutes, resulting in a rate of change of aspect angle of 0.6 degrees/s, or 0.0104 rad/s. This translates to an error in radial velocity of roughly 0.38 m/s. Note, these numbers are only indicative, however they show that only the glint error in range is significant. At long ranges the glint error in azimuth and elevation become negligible, these are only significant for close range targets. Subsequently the radial velocity error becomes negligible because the satellite does not manoeuvre, this error becomes significant for fast manoeuvring target such as fighters and missiles, or targets with rotating components such as drones and helicopters. Going forward, only the glint error in range is considered.

Instrumental error

As seen from the noise error, the accuracy is greatly dependant on the signal to noise ratio. These equations describe that if one would achieve an infinite signal-to-noise ratio, that the standard deviation would go to zero, providing perfect measurements. This is not the case however. A radar system has more error sources such as deformation of the antenna due to the Sun, quantisation errors in the signal processing, internal jitter, lag, sample rate errors and more [69]. These are all bundled into the instrument error. This means that the for an infinite signal-to-noise ratio, a certain minimum error will be achieved, which is the instrument error. This error is very complex and system dependant. For this study a simplified approach is used which will be explained in more detail in subsection 3.2.2.

2.2. Orbital Dynamics

This section presents a physical understanding of satellite motion around Earth. For this study a numerical model is utilised, which will simulate the motion of satellites around Earth.

2.2.1. Reference frames

The measurements and forces acting on the satellite are measured and calculated in different reference frames, thus these need to be well defined. According to Wakker [70], a reference frame consists of a set of identifiable fiducial points on the sky along with their coordinates, which specify how the origin and orientation of a celestial body can be incorporated to construct a system of reference. For this study, four different reference frames are used for this study, which are mentioned below.

The dynamics of a satellite are defined in an *Earth-centred inertial* (ECI) frame while the observations by the ground station are done from a fixed point on Earth's surface known as a topocentric frame. The topocentric frame however, depends on the *Earth-centred Earth-fixed* (ECEF) frame. A local orbital frame is also used to make the results more intuitive, which is with respect to the spacecraft flight direction.

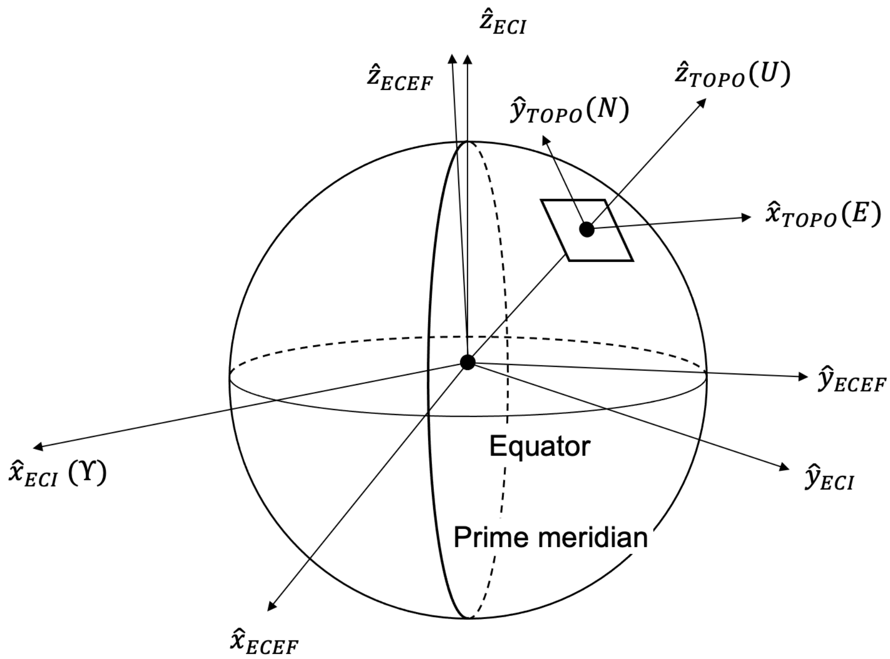

Figure 2.6: Diagram illustrating the ECI, ECEF and topocentric frames.

Earth-Centred Inertial (ECI)

An Earth-Centred inertial frame, as the name suggests is an inertial frame with the origin at the Earth's centre. The dynamics of the spacecraft are most easily defined in this frame. The J2000 (or EME2000) frame is used as the inertial frame, which is independent of Earth's rotation. The X-axis coincides with the intersection of the equatorial and ecliptic planes, known as the vernal equinox (♈). This intersection changes over time due to the precession and nutation of Earth. The most commonly used ECI frame is the J2000 frame, which defines the x-axis to be pointed towards the vernal equinox measured on 1st January 2000 at 12:00 terrestrial time. The z-axis is normal to the mean equator in the north direction and the y-axis completes the right-hand rule [71], forming an orthogonal basis. This frame is depicted in Figure 2.6.

Earth-Centred Earth-Fixed (ECEF)

An Earth-centred Earth-fixed reference frame defines the position of an object with respect to Earth-fixed axes with the center of Earth as the origin. In other words, the frame rotates along with the rotation of Earth. The x-axis coincides with the prime meridian and the equator, the z-axis coincides with the Earth rotation axis and the y-axis completed the right-hand rule. This frame is depicted in Figure 2.6.

For this study the *International Terrestrial Reference Frame* (ITRF) is used. This is a reference frame that takes in *Earth Orientation Parameters* (EOPs) for Earth's rotation, nutation, precession and more [72]. The ITRF uses EOPs from the *International Earth Rotation and Reference Systems Service* (IERS) from 2010 [73].

Topocentric frame

The topocentric frame is based on the position of a ground station on Earth's surface, in the case of this study, the SMART-L MM/N radar tower in Hengelo. To define a ground station on Earth, a reference for Earth has to be defined. This is done using an ellipsoid and the WGS84 conventions for the equatorial radius and flattening of Earth [74]. The topocentric frame has its x-axis heading East, along the local parallel, the y-axis heading North and the z-axis normal to the local horizontal plane. This convention is also known as an ENU frame (east, north, up frame). This frame is depicted in Figure 2.6.

LVLH frame (local orbital frame)

A spacecraft also has a local reference frame, along the direction of the trajectory. For this study, it is used to make the errors between the reference trajectory and the estimated trajectory more intuitive. In the LVLH (local-vertical, local-horizontal) frame, the x-axis is pointing towards the spacecraft's position vector (radial) from the centre of Earth. The z-axis points normal to the orbital plane, along the angular momentum vector (cross-track). The y-axis completes the orthonormal coordinate system (in-track), as illustrated in Figure 2.7

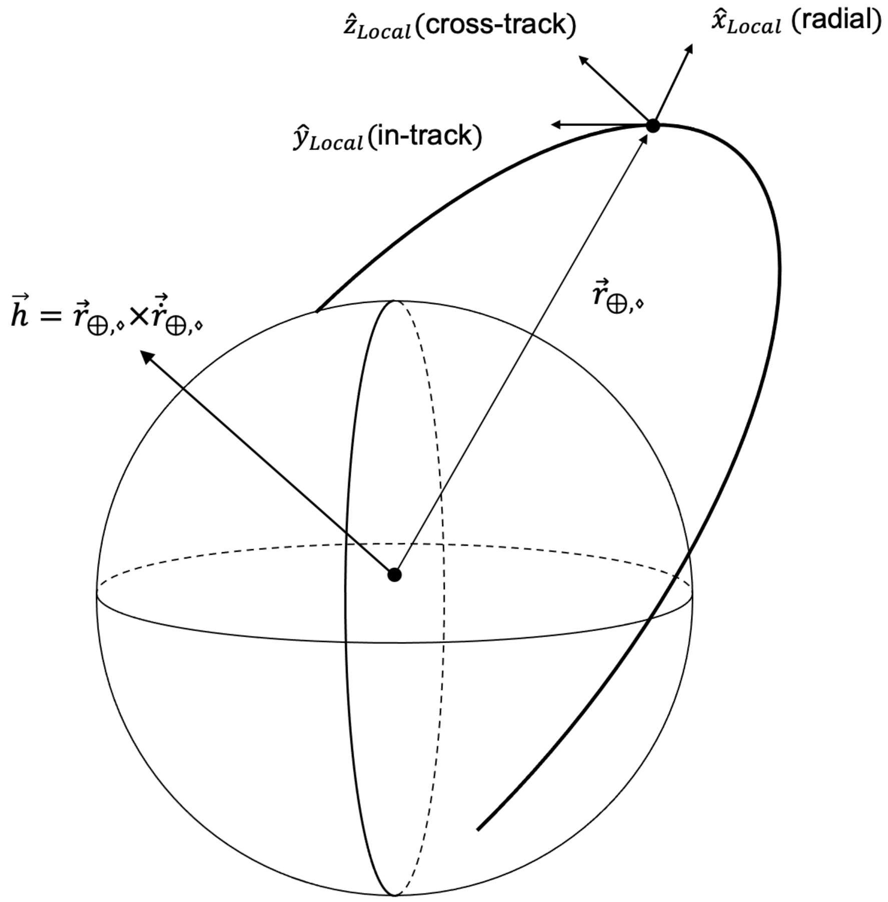

Figure 2.7: Diagram illustrating the local orbital frame.

2.2.2. Forces acting on the spacecraft

People tend to view the universe as highly regular and predictable. Yet accurate observational data often reveals unexplained irregularities of motion superimposed on the more regular motion of the celestial bodies. The real motion of satellites does not conform to the assumption of two-body dynamics as described by Kepler [9]. The actual motion of a satellite will vary due to the perturbations caused by other bodies such as the Sun and the Moon. The usual perturbing forces that are considered for an orbit problem are asphericity of the central body, atmospheric drag and lift, third body effects, solar-radiation pressure, thrust, magnetic fields, solid-Earth and ocean tides, Earth re-radiation (albedo), relativistic effects and others [14]. For this study the asphericity of Earth, atmospheric drag, solar-radiation pressure and third body effects are considered, as they are most dominant.

Gravity

Newton's universal law of gravitation states that two particles attract each other with a force directly proportional to their masses and inversely proportional to the square of the distance between them. The point-mass acceleration of the Earth is most dominant acceleration acting on the spacecraft and is expressed by Equation 2.25 [75].

$$\ddot{\vec{r}} = -\frac{\mu}{r^3}\vec{r} \tag{2.25}$$

where μ is the gravitational parameter of Earth (398600.4418 km^3/s^2), $\vec{r}$ is the objects position vector. Derivations made from Equation 2.25 result in a Kepler orbit [70].

However, Earth is not a perfect homogeneous sphere or a point-mass, a satellite will experience a different acceleration depending on its position. For example, above the Himalaya mountain range, it will experience a larger acceleration because there is relatively more mass. The opposite holds true if a satellite would fly above an ocean. The absence of mass makes the satellite experience a smaller acceleration. To analyse these conservative accelerations, use is made of gradients (indicated by the del operator ∇). The gradient gives an acceleration if the scalar function is a potential function related to a specific potential energy, such as the potential function of a central body's gravity field. The term *geopotential* is often used for this aspherical potential when the central body is the Earth.

As an example, the gravitational potential for a spherical central body is

$$U_{sph} = \frac{\mu}{r}$$

The gradient takes the partial derivatives in each axis, in Cartesian coordinates this becomes,

$$\nabla U_{sph} = \frac{\partial U_{sph}}{\partial x}\hat{\imath} + \frac{\partial U_{sph}}{\partial y}\hat{\jmath} + \frac{\partial U_{sph}}{\partial z}\hat{k}$$

where $\hat{\imath}, \hat{\jmath}, \hat{k}$ denote the unit vectors along the axes of the coordinate system, with position vector $\vec{r} = x\hat{\imath} + y\hat{\jmath} + z\hat{k}$ and magnitude $r = \sqrt{x^2 + y^2 + z^2}$. The acceleration becomes,

$$\nabla U_{sph} = \frac{1}{2}\frac{\mu}{(x^2 + y^2 + z^2)^{3/2}}\left[2x\hat{\imath} + 2y\hat{\jmath} + 2z\hat{k}\right] = -\frac{\mu}{r^3}\vec{r}$$

Which, as expected, is the two-body acceleration for a satellite. Hence,

$$\ddot{\vec{r}} = \nabla U \tag{2.26}$$

Vallado derived the aspherical-potential function for Earth in his book, following the methods of Roy [76], Kaplan [77] and Fitzpatrick [78]. He derived the following equation for the geopotential,

$$U = \frac{\mu}{r}\left[1 + \sum_{l=2}^{\infty}\sum_{m=0}^{l}\left(\frac{R_{\oplus}}{r}\right)P_{l,m}\left[\sin\left(\phi_{gc,sat}\right)\right]\left\{C_{l,m}\cos\left(m\lambda_{sat}\right) + S_{l,m}\sin\left(m\lambda_{sat}\right)\right\}\right] \tag{2.27}$$

where l and m are respectively the *degree* and *order*. These are used for the associated Legendre polynomials $P_{l,m}\left[\sin(\phi_{gc,sat})\right]$ introduced by Lambeck [79], where $\phi_{gc,sat}$ is the geocentric latitude of the satellite. The Legendre polynomials are defined as,

$$P_{l,m}[\gamma] = \frac{1}{2^l l!}\left(1-\gamma^2\right)^{m/2}\frac{d^{l+m}}{d\gamma^{l+m}}\left(\gamma^2 - 1\right)^l \tag{2.28}$$

An example of such an associated Legendre function with degree 2 and order 0 is,

$$P_{2,0} = \frac{1}{2}\left\{3\sin^2\left(\phi_{gc,sat}\right) - 1\right\} \tag{2.29}$$

The coefficients $C_{l,m}$ and $S_{l,m}$ in Equation 2.27 represent the mathematical modelling for Earth's shape using spherical harmonics. These coefficients are determined from observations, which is a common method in developing gravitational fields today [14].

From this potential function, using Equation 2.26, the acceleration in Cartesian coordinates can be calculated,

$$\ddot{\vec{r}} = \frac{\partial U}{\partial r}\left(\frac{\partial r}{\partial \vec{r}}\right)^T + \frac{\partial U}{\partial \phi_{gc,sat}}\left(\frac{\partial \phi_{gc,sat}}{\partial \vec{r}}\right)^T + \frac{\partial U}{\partial \lambda_{sat}}\left(\frac{\lambda_{sat}}{\partial \vec{r}}\right)^T \tag{2.30}$$

The J_2 perturbation is a thousand times stronger than the subsequent J_3 effect [14]. Because of Earth's rotation, the Earth is flattened making the equatorial radius larger than the polar radius. As a result of this equatorial bulge there is a larger gravitational acceleration, as the satellite passes the equator.

Third body effects

Not only Earth, but all other celestial bodies exert a gravitational force on the satellite. The strongest third body perturbations are caused by the Sun and the Moon [14]. These bodies can also be modelled using spherical harmonics, however for long distances these local anomalies become inert. For this reason, point mass gravity is assumed for third bodies.

$$\ddot{\vec{r}}_{3,\diamond} = \frac{\mu_3}{|\vec{r}_{3,\diamond}|^3}\vec{r}_{3,\diamond} \tag{2.31}$$

where subscript 3 denotes the third body.

Atmospheric drag

Atmospheric drag is caused by the interaction of between the particles in the atmosphere and the satellite. Drag is a non-conservative force because the energy is not conserved, there is a loss of energy due to this friction. The equation for aerodynamic drag is,

$$\ddot{\vec{r}}_{drag} = \frac{\rho\,|\vec{v}_{rel}|^2\,AC_D}{2m}\hat{v}_{rel} \tag{2.32}$$

where, ρ is the atmospheric density in kg/m^3, $\vec{v}_{rel}$ is the velocity relative to the atmosphere. A is the cross-sectional area in m^2, C_D is the drag coefficient (typically around 2.2, using a flat plate model) and m is the spacecraft mass [14].

Solar-radiation pressure

Solar-radiation pressure is similar to atmospheric drag because they are both non-conservative forces. The radiation of the Sun exerts a force on the satellite causing a perturbation in the path. The equation for solar radiation pressure is,

$$\ddot{\vec{r}}_{srp} = -\frac{p_{srp}C_R A_\odot}{m}\frac{\vec{r}_{\diamond,\odot}}{|\vec{r}_{\diamond,\odot}|} \tag{2.33}$$

where p_{srp} is the solar-radiation pressure (roughly $4.57 \times 10^{-6} N/m^2$), C_R is the reflectivity, $A_\odot$ is the exposed area of the Sun, $\vec{r}_{\diamond,\odot}$ is the position vector from the spacecraft to the Sun and m is the spacecraft mass [14].

2.3. Orbit Determination

Satellite orbit determination is the process to obtain knowledge of the satellites motion relative to the center of mass of the Earth [37]. The motion of the satellite is determined by the state of the spacecraft at a certain time,

$$\vec{\mathbb{X}}(t) = \begin{bmatrix} x & y & z & \dot{x} & \dot{y} & \dot{z} \end{bmatrix} \tag{2.34}$$

The difficulty in this problem is that the state cannot be directly observed and there is a nonlinear relationship between the observations and the state. Next to that, a radar system can measure four different parameters, each subject to measurement errors.

In the current study, four distinct orbit determination techniques are employed: the *batch least squares estimator* (BLSE), the *extended Kalman filter* (EKF), the *unscented batch estimator* (UBE), and the *unscented Kalman filter* (UKF). The initial two techniques, BLSE and EKF, rely on traditional linearisation methods to approximate the state vector. In contrast, the UBE and UKF employ the unscented transform, which does not necessitate linearisation and is thereby better suited to handle the nonlinear nature of the state estimation problem.

The distinction is further made in how these techniques process measurements. Batch estimators, including BLSE and UBE, process all available measurements in a single batch. This approach is predominantly utilised in offline settings, such as the retrospective analysis of satellite orbits, where all data can be compiled and analysed collectively. Conversely, sequential estimators like the EKF and UKF update the state vector recursively, integrating new data as it becomes available. This method is used in real-time applications, such as satellite guidance, navigation, and control systems, where immediacy and ongoing adjustment are crucial.

2.3.1. Conventional Estimation Techniques

In this subsection, the BLSE and the EKF are discussed. Both algorithms linearise the observation and dynamics models with a Taylor series expansion. First the linearisation process is discussed, subsequently the batch least squares estimator (BLSE) and finally the extended Kalman filter (EKF).

Linearisation of Nonlinear Orbital Dynamics

As it is well recognised, the orbital dynamics problem is inherently nonlinear. Nonlinear systems, such as the dynamics of a spacecraft, can often be approximated by linear systems using linearization techniques like the Taylor Series expansion. The dynamics of a spacecraft are governed by a nonlinear differential equation represented as follows:

$$\dot{\vec{\mathbb{X}}} = F(\vec{\mathbb{X}}, t) \tag{2.35}$$

where $\vec{\mathbb{X}}$ is the state vector of the spacecraft, and $F(\vec{\mathbb{X}}, t)$ is the dynamics model that describes how the state changes over time. Observations related to the state vector are modelled by the equation:

$$\vec{Y_i} = G(\vec{\mathbb{X}}_i, t_i) + \epsilon_i \tag{2.36}$$

where $\vec{Y_i}$ represents the set of observations, $G(\vec{\mathbb{X}}_i, t_i)$ is the observation model converting the spacecraft state into the measurement space, and ϵ_i denotes the measurement error. To facilitate linearization, a state deviation vector $\vec{x}$ and an observation deviation vector $\vec{y}$ are defined as:

$$\vec{x} = \vec{\mathbb{X}}_{\text{true}} - \vec{\mathbb{X}}_{\text{ref}}, \quad \vec{y} = \vec{Y}_{\text{true}} - G(\vec{\mathbb{X}}, t) \tag{2.37}$$

The change in the state deviation vector is given by:

$$\dot{\vec{x}} = \dot{\vec{\mathbb{X}}}_{\text{true}} - \dot{\vec{\mathbb{X}}}_{\text{ref}} \tag{2.38}$$

At the initial epoch, the estimated deviation is $\hat{x}_0$, leading to:

$$\vec{\mathbb{X}}_{\text{est}} = \vec{\mathbb{X}}_{\text{ref,0}} + \hat{x}_0 \tag{2.39}$$

The Taylor Series expansion of the true state dynamics around the reference trajectory can be expressed as:

$$\dot{\vec{\mathbb{X}}}_{\text{true}} = \dot{\vec{\mathbb{X}}}_{\text{ref}} + \left[\frac{\partial \dot{\vec{\mathbb{X}}}}{\partial \vec{\mathbb{X}}}\right] \vec{x} + \frac{1}{2}\left[\frac{\partial^2 \dot{\vec{\mathbb{X}}}}{\partial \vec{\mathbb{X}}^2}\right] \vec{x}^2 + \frac{1}{6}\left[\frac{\partial^3 \dot{\vec{\mathbb{X}}}}{\partial \vec{\mathbb{X}}^3}\right] \vec{x}^3 + \dots \tag{2.40}$$

By retaining only the linear term of the Taylor Series expansion, the linearized dynamics model is obtained:

$$\dot{\vec{\mathbb{X}}}_{\text{true}} - \dot{\vec{\mathbb{X}}}_{\text{ref}} \approx \left[\frac{\partial \dot{\vec{\mathbb{X}}}}{\partial \vec{\mathbb{X}}}\right] \vec{x} \tag{2.41}$$

$$\dot{\vec{x}} \approx \left[\frac{\partial \dot{\vec{\mathbb{X}}}}{\partial \vec{\mathbb{X}}}\right] \vec{x} \tag{2.42}$$

This can be written in a form that is used in the BLSE and EKF:

$$\dot{\vec{x}} = \boldsymbol{A}(t)\vec{x}, \quad \boldsymbol{A}(t) = \left[\frac{\partial \dot{\vec{\mathbb{X}}}}{\partial \vec{\mathbb{X}}}\right] \tag{2.43}$$

For an illustrative example, consider the force model of a point mass under central gravitational influence, which is given by:

$$\ddot{\vec{r}}_{\oplus,\diamond} = -\frac{\mu_\oplus}{|\vec{r}_{\oplus,\diamond}|^3} \vec{r}_{\oplus,\diamond} \tag{2.44}$$

Here, $\mu_\oplus$ denotes the standard gravitational parameter for Earth, and $\vec{r}_{\oplus,\diamond}$ represents the position vector from Earth to the spacecraft. The derivative of the state vector $\vec{\mathbb{X}}$ is expressed as:

$$\dot{\vec{\mathbb{X}}} = \begin{bmatrix} \dot{x} \\ \dot{y} \\ \dot{z} \\ \ddot{x} \\ \ddot{y} \\ \ddot{z} \end{bmatrix} = \begin{bmatrix} \dot{x}_{\oplus,\diamond} \\ \dot{y}_{\oplus,\diamond} \\ \dot{z}_{\oplus,\diamond} \\ -\frac{\mu_\oplus}{|\vec{r}_{\oplus,\diamond}|^3} \vec{x}_{\oplus,\diamond} \\ -\frac{\mu_\oplus}{|\vec{r}_{\oplus,\diamond}|^3} \vec{y}_{\oplus,\diamond} \\ -\frac{\mu_\oplus}{|\vec{r}_{\oplus,\diamond}|^3} \vec{z}_{\oplus,\diamond} \end{bmatrix} \tag{2.45}$$

Resulting in the $\boldsymbol{A}(t)$-matrix as,

$$\boldsymbol{A}(t)=\begin{bmatrix}\frac{\partial \dot{x}}{\partial x} & \frac{\partial \dot{x}}{\partial y} & \frac{\partial \dot{x}}{\partial z} & \frac{\partial \dot{x}}{\partial \dot{x}} & \frac{\partial \dot{x}}{\partial \dot{y}} & \frac{\partial \dot{x}}{\partial \dot{z}}\\ \frac{\partial \dot{y}}{\partial x} & \frac{\partial \dot{y}}{\partial y} & \frac{\partial \dot{y}}{\partial z} & \frac{\partial \dot{y}}{\partial \dot{x}} & \frac{\partial \dot{y}}{\partial \dot{y}} & \frac{\partial \dot{y}}{\partial \dot{z}}\\ \frac{\partial \dot{z}}{\partial x} & \frac{\partial \dot{z}}{\partial y} & \frac{\partial \dot{z}}{\partial z} & \frac{\partial \dot{z}}{\partial \dot{x}} & \frac{\partial \dot{z}}{\partial \dot{y}} & \frac{\partial \dot{z}}{\partial \dot{z}}\\ \frac{\partial \ddot{x}}{\partial x} & \frac{\partial \ddot{x}}{\partial y} & \frac{\partial \ddot{x}}{\partial z} & \frac{\partial \ddot{x}}{\partial \dot{x}} & \frac{\partial \ddot{x}}{\partial \dot{y}} & \frac{\partial \ddot{x}}{\partial \dot{z}}\\ \frac{\partial \ddot{y}}{\partial x} & \frac{\partial \ddot{y}}{\partial y} & \frac{\partial \ddot{y}}{\partial z} & \frac{\partial \ddot{y}}{\partial \dot{x}} & \frac{\partial \ddot{y}}{\partial \dot{y}} & \frac{\partial \ddot{y}}{\partial \dot{z}}\\ \frac{\partial \ddot{z}}{\partial x} & \frac{\partial \ddot{z}}{\partial y} & \frac{\partial \ddot{z}}{\partial z} & \frac{\partial \ddot{z}}{\partial \dot{x}} & \frac{\partial \ddot{z}}{\partial \dot{y}} & \frac{\partial \ddot{z}}{\partial \dot{z}}\end{bmatrix} \tag{2.46}$$

Upon calculating all the partial derivatives, the final $\boldsymbol{A}(t)$-matrix is obtained:

$$\boldsymbol{A}(t)=\begin{bmatrix}0 & 0 & 0 & 1 & 0 & 0\\ 0 & 0 & 0 & 0 & 1 & 0\\ 0 & 0 & 0 & 0 & 0 & 1\\ -\frac{\mu_\oplus}{|\vec{r}|^3}+\frac{3\mu_\oplus x^2}{|\vec{r}|^5} & \frac{3\mu_\oplus xy}{|\vec{r}|^5} & \frac{3\mu_\oplus xz}{|\vec{r}|^5} & 0 & 0 & 0\\ \frac{3\mu_\oplus yx}{|\vec{r}|^5} & -\frac{\mu_\oplus}{|\vec{r}|^3}+\frac{3\mu_\oplus y^2}{|\vec{r}|^5} & \frac{3\mu_\oplus yz}{|\vec{r}|^5} & 0 & 0 & 0\\ \frac{3\mu_\oplus zx}{|\vec{r}|^5} & \frac{3\mu_\oplus zy}{|\vec{r}|^5} & -\frac{\mu_\oplus}{|\vec{r}|^3}+\frac{3\mu_\oplus z^2}{|\vec{r}|^5} & 0 & 0 & 0\end{bmatrix} \tag{2.47}$$

The linearization process can also be applied to the observation model from Equation 2.36, leading to the following formulation:

$$\vec{Y}_k=\tilde{\boldsymbol{H}}_k\boldsymbol{\Phi}(t_k,t_0)\vec{\mathbb{X}}_0+\vec{\epsilon}_k, \quad \text{where } \tilde{\boldsymbol{H}}_k=\left[\frac{\partial G\left(\vec{\mathbb{X}}_k\right)}{\partial \vec{\mathbb{X}}_k}\right]_{\mathbb{X}_{\text{ref}}} \tag{2.48}$$

Here, $\tilde{\boldsymbol{H}}_k$ represents the observation mapping matrix, and $\boldsymbol{\Phi}(t_k,t_0)$ is the state transition matrix (STM) that maps the state from an initial time t_0 to a time t_k:

$$\vec{\mathbb{X}}_k=\boldsymbol{\Phi}(t_k,t_0)\vec{\mathbb{X}}_0 \tag{2.49}$$

The STM is derived from the $\boldsymbol{A}(t)$-matrix used in the dynamics model, governed by:

$$\dot{\boldsymbol{\Phi}}(t_k,t_0)=\boldsymbol{A}(t)\boldsymbol{\Phi}(t_k,t_0) \tag{2.50}$$

Given the $\boldsymbol{A}(t)$-matrix and the STM, the derivative can be calculated and integrated using the dynamics model. This will result in the STM for the next time step. The radar system measures range, azimuth, elevation and radial velocity. Accordingly, the measurement vector is defined as:

$$\vec{Y}_k=\begin{bmatrix}R_k & \phi_k & \theta_k & V_{r_k}\end{bmatrix}^T \tag{2.51}$$

where R is the range, ϕ the azimuth, θ the elevation, and V_r the radial velocity. The corresponding observation mapping matrix, $\tilde{\boldsymbol{H}}_k$, is then outlined:

$$\tilde{\boldsymbol{H}}_k = \begin{bmatrix} \frac{\partial R}{\partial x} & \frac{\partial R}{\partial y} & \frac{\partial R}{\partial z} & \frac{\partial R}{\partial \dot{x}} & \frac{\partial R}{\partial \dot{y}} & \frac{\partial R}{\partial \dot{z}} \\ \frac{\partial \phi}{\partial x} & \frac{\partial \phi}{\partial y} & \frac{\partial \phi}{\partial z} & \frac{\partial \phi}{\partial \dot{x}} & \frac{\partial \phi}{\partial \dot{y}} & \frac{\partial \phi}{\partial \dot{z}} \\ \frac{\partial \theta}{\partial x} & \frac{\partial \theta}{\partial y} & \frac{\partial \theta}{\partial z} & \frac{\partial \theta}{\partial \dot{x}} & \frac{\partial \theta}{\partial \dot{y}} & \frac{\partial \theta}{\partial \dot{z}} \\ \frac{\partial V_r}{\partial x} & \frac{\partial V_r}{\partial y} & \frac{\partial V_r}{\partial z} & \frac{\partial V_r}{\partial \dot{x}} & \frac{\partial V_r}{\partial \dot{y}} & \frac{\partial V_r}{\partial \dot{z}} \end{bmatrix} \tag{2.52}$$

These radar coordinates are related to the spacecraft state through the following relationships:

$$\begin{aligned} R &= \sqrt{x_T^2 + y_T^2 + z_T^2} \\ \phi &= \text{arctan}\left(\frac{y_T}{x_T}\right) \\ \theta &= \text{arcsin}\left(\frac{z_T}{\sqrt{x_T^2 + y_T^2 + z_T^2}}\right) \\ V_r &= \frac{x_T \dot{x}_T + y_T \dot{y}_T + z_T \dot{z}_T}{\sqrt{x_T^2 + y_T^2 + z_T^2}} \end{aligned} \tag{2.53}$$

Note that these position and velocity vectors are relative from the ground station to the spacecraft, denoted by subscript T. If the position of the spacecraft is known in ECI and the position of the ground station in ECI, the relative position would be,

$$x_T = x_\diamond - x_{\text{gs}} \tag{2.54}$$

By calculating the partial derivatives, the observation matrix $\tilde{\boldsymbol{H}}$ is computed. Its derivation is explained in Appendix B. For the notation of the $\tilde{\boldsymbol{H}}$-matrix, no subscripts are used for readability. However, these positions are defined in the topocentric frame, meaning that the same logic applies as for Equation 2.53, using Equation 2.54.

$$\tilde{\boldsymbol{H}} = \begin{bmatrix} \frac{x}{R} & \frac{y}{R} & \frac{z}{R} & 0 & 0 & 0 \\ \frac{y}{\sqrt{x^2+y^2}} & -\frac{x}{\sqrt{x^2+y^2}} & 0 & 0 & 0 & 0 \\ -\frac{xz}{R^2\sqrt{x^2+y^2}} & -\frac{yz}{R^2\sqrt{x^2+y^2}} & \frac{\sqrt{x^2+y^2}}{R^2} & 0 & 0 & 0 \\ \frac{-xy\dot{y} - xz\dot{z} + \dot{x}\left(y^2+z^2\right)}{R^3} & \frac{-xy\dot{x} - yz\dot{z} + \dot{y}\left(x^2+z^2\right)}{R^3} & \frac{-zx\dot{x} - zy\dot{y} + \dot{z}\left(x^2+y^2\right)}{R^3} & \frac{x}{R} & \frac{y}{R} & \frac{z}{R} \end{bmatrix} \tag{2.55}$$

Batch Least Squares estimator

The goal of the least squares estimator is to minimise the sum of the squares of the calculated observation residuals. This method was first proposed by Gauss in 1809 [13] and is still widely used today [37]. However, the method described by Gauss does not consider the quality of the observations, the correlation between observations and any other statistical information.

Hence, the minimum variance batch least squares algorithm is used.

The *batch least squares estimator* (BLSE) starts by defining an initial guess $\vec{\mathbb{X}}_0$ and the initial covariance $\boldsymbol{P}_0$. The initial covariance indicates the accuracy of the initial guess. It is assumed that the initial state errors are uncorrelated. Then the state transition matrix $\boldsymbol{\Phi}$ at time t_0 is defined as an identity matrix of size $n \times n$, where n is the number of elements in the state vector. For orbit determination $n = 6$. Also, the state deviation estimate $\hat{x}_0$ is defined as a zero vector.

$$\boldsymbol{\Phi}(t_0, t_0) = I_{6\times6}, \quad \bar{x}_0 = \hat{x}_0 = \mathbf{0}_{6\times1} \tag{2.56}$$

Now the initialisation for the first iteration can be done by defining the normal equations,

$$\boldsymbol{\Lambda} = \boldsymbol{P}_0^{-1} \tag{2.57}$$

$$\boldsymbol{N} = \boldsymbol{\Lambda}\bar{x}_0 \tag{2.58}$$

With the initialisation for the first iteration done, the next step is to read the first observation $\vec{Y}_k$ at time t_k with covariance matrix $\boldsymbol{R}_k$. This covariance matrix yields the uncertainties of the measurements. It is assumed that the covariances are uncorrelated in time, which results in a measurement vector and covariance matrix as such,

$$\vec{Y}_k = \begin{bmatrix} R_k \\ \phi_k \\ \theta_k \\ V_{r,k} \end{bmatrix}, \quad \boldsymbol{R}_k = \begin{bmatrix} \sigma_R^2 & 0 & 0 & 0 \\ 0 & \sigma_\phi^2 & 0 & 0 \\ 0 & 0 & \sigma_\theta^2 & 0 \\ 0 & 0 & 0 & \sigma_{V_r}^2 \end{bmatrix} \tag{2.59}$$

The reference state and state transition matrix are then combined and propagated from the previous time step t_{k-1} to the subsequent timestep t_k using a dynamics model. The outcome of this propagation is a state $\vec{\mathbb{X}}_k$ and a new state transition matrix $\boldsymbol{\Phi}\left(t_{k-1}, t_k\right)$. The next step is to calculate the observation deviation vector $\vec{y}_k$, the observation-state matrix $\tilde{\boldsymbol{H}}_k$ and the observation matrix $\boldsymbol{H}_k$,

$$\vec{y}_k = \vec{Y}_k - G\left(\vec{\mathbb{X}}_k, t_k\right) \tag{2.60}$$

$$\tilde{\boldsymbol{H}}_k = \frac{\partial G\left(\vec{\mathbb{X}}, t_k\right)}{\partial \vec{\mathbb{X}}} \tag{2.61}$$

$$\boldsymbol{H}_k = \tilde{\boldsymbol{H}}_k \boldsymbol{\Phi}\left(t_{k-1}, t_k\right) \tag{2.62}$$

The function $G\left(\vec{\mathbb{X}}_k, t_k\right)$ transforms the propagated Cartesian state to the measurement space. The measurements are made in a topocentric frame, whilst the Cartesian spacecraft state is in the inertial frame, meaning a frame transformation is necessary for this step. Now the normal equations can be updated,

$$\boldsymbol{\Lambda}_k = \boldsymbol{\Lambda}_{k-1} + \boldsymbol{H}_k^T \boldsymbol{R}_k^{-1} \boldsymbol{H}_k \tag{2.63}$$

$$\boldsymbol{N}_k = \boldsymbol{N}_{k-1} + \boldsymbol{H}_k^T \boldsymbol{R}_k^{-1} \vec{y}_k \tag{2.64}$$

The calculation of these normal equations are done for every measurement. After all the measurements are processed an estimate is made on the initial state. First, the new initial covariance $\boldsymbol{P}_0$ is calculated and then the state deviation $\hat{x}_0$. For convenience, the subscript j is introduced to indicate the iteration number.

$$(\boldsymbol{P}_0)_j = \boldsymbol{\Lambda}^{-1} \tag{2.65}$$

$$(\hat{x}_0)_j = \boldsymbol{P}_0 \boldsymbol{N} \tag{2.66}$$

With the state deviation vector $\hat{x}_0$, the initial state estimated is updated,

$$(\vec{\mathbb{X}}_0)_j = (\vec{\mathbb{X}}_0)_{j-1} + (\hat{x}_0)_j \tag{2.67}$$

$$(\bar{x}_0)_j = (\bar{x}_0)_{j-1} - (\hat{x}_0)_j \tag{2.68}$$

Finally, the algorithm will check for convergence. The solution is considered to have converged if the relative change in the root mean square (RMS) of the residuals between iterations is below a specified threshold ϵ_{rms}:

$$\frac{|\text{RMS}_j - \text{RMS}_{j-1}|}{\text{RMS}_{j-1}} < \epsilon_{\text{rms}}, \quad \left(\epsilon_{\text{rms}} = 1 \times 10^{-4}\right) \tag{2.69}$$

If convergence is not achieved, and the maximum number of iterations k_{max} is reached, the algorithm terminates. Otherwise, a new iteration will start. Once convergence is achieved, $\vec{\mathbb{X}}_0$ will be the state estimate together with the uncertainty captured in the initial state covariance $\boldsymbol{P}_0$.

Extended Kalman Filter

The *extended Kalman filter* (EKF) is a sequential estimator. This means that it estimates the spacecraft state, as new measurements are being processed. The EKF starts by defining the initial guess $\vec{\mathbb{X}}_0$ and the initial covariance $\boldsymbol{P}_0$. The initial covariance indicates the accuracy of the initial guess. It is assumed that the initial state errors are uncorrelated. Then the state transition matrix $\boldsymbol{\Phi}$ at time t_0 is defined as an identity matrix of size $n \times n$, for orbit determination $n = 6$. Also, state deviation estimate $\hat{x}_0$ is defined as a zero vector.

$$\boldsymbol{\Phi}(t_0, t_0) = I_{6\times6}, \quad \bar{x}_0 = \hat{x}_0 = \mathbf{0}_{6\times1} \tag{2.70}$$

The next step is to read the first observation $\vec{Y}_k$ at time t_k with covariance matrix $\boldsymbol{R}_k$. It is assumed that the covariances are uncorrelated in time, similar to the BLSE. The reference state and state transition matrix are then combined and propagated from the previous time step t_{k-1} to the subsequent timestep t_k using a dynamics model. The outcome of this propagation is a state $\vec{\mathbb{X}}_k$ and a new state transition matrix $\boldsymbol{\Phi}\left(t_{k-1}, t_k\right)$. Next is the time update of the state estimate and the covariance,

$$\bar{x}_k = \boldsymbol{\Phi}\left(t_{k-1}, t_k\right) \hat{x}_{k-1} \tag{2.71}$$

$$\bar{\boldsymbol{P}}_k = \boldsymbol{\Phi}\left(t_{k-1}, t_k\right) \boldsymbol{P}_{k-1} \boldsymbol{\Phi}\left(t_{k-1}, t_k\right)^T + \boldsymbol{\Gamma}\boldsymbol{Q}\boldsymbol{\Gamma}^T \tag{2.72}$$

Note, the term $\boldsymbol{\Gamma}\boldsymbol{Q}\boldsymbol{\Gamma}^T$ is known as the state noise compensation, which ensures that the estimator does not saturate. Filter saturation occurs when the covariance matrix, $\bar{\boldsymbol{P}}$, is excessively small, indicating an overly confident trust in the propagated state. This overconfidence leads to the disregard of new measurements. The introduction of a *state noise compensation* (SNC) matrix, by augmenting $\bar{\boldsymbol{P}}$, ensures that new observations are incorporated. However, if the SNC's magnitude is too large, the filter may entirely dismiss the propagated state, relying solely on observations. The state noise compensation consists of a process noise transition matrix $\boldsymbol{\Gamma}$ and a process noise covariance matrix $\boldsymbol{Q}$. The process noise covariance matrix contains the variances of unmodelled accelerations σ_a^2 and the process noise transition matrix maps these accelerations back to velocity and position as such,

$$\boldsymbol{\Gamma} = \begin{bmatrix} \frac{\Delta t^2}{2} & 0 & 0 \\ 0 & \frac{\Delta t^2}{2} & 0 \\ 0 & 0 & \frac{\Delta t^2}{2} \\ \Delta t & 0 & 0 \\ 0 & \Delta t & 0 \\ 0 & 0 & \Delta t \end{bmatrix}, \quad \boldsymbol{Q} = \begin{bmatrix} \sigma_{\ddot{x}}^2 & 0 & 0 \\ 0 & \sigma_{\ddot{y}}^2 & 0 \\ 0 & 0 & \sigma_{\ddot{z}}^2 \end{bmatrix} \tag{2.73}$$

The next step is to compute the observation deviation vector $\vec{y}_k$, the observation-state matrix $\tilde{\boldsymbol{H}}_k$ and the Kalman gain $\boldsymbol{K}_k$.

$$\vec{y}_k = \vec{Y}_k - G\left(\vec{\mathbb{X}}_{\text{ref},k}, t_k\right) \tag{2.74}$$

$$\tilde{\boldsymbol{H}}_k = \left[\frac{\partial G\left(\vec{\mathbb{X}}, t_k\right)}{\partial \vec{\mathbb{X}}}\right]_{\mathbb{X}_{\text{ref}}} \tag{2.75}$$

$$\boldsymbol{K}_k = \bar{\boldsymbol{P}}_k \tilde{\boldsymbol{H}}_k^T \left(\tilde{\boldsymbol{H}}_k \bar{\boldsymbol{P}}_k \tilde{\boldsymbol{H}}_k^T + \boldsymbol{R}_k\right)^{-1} \tag{2.76}$$

The function $G\left(\vec{\mathbb{X}}_k, t_k\right)$ transforms the propagated Cartesian state to the measurement space. The measurements are made in a topocentric frame, whilst the Cartesian spacecraft state is in the inertial frame, meaning a frame transformation is necessary for this step. By taking the partial derivatives of this function with respect to the Cartesian state, the observation-state matrix $\tilde{\boldsymbol{H}}_k$ is derived. The Kalman gain is a measure of how much the filter will accept the new measurements. If $\boldsymbol{R}_k$ is small relative to $\bar{\boldsymbol{P}}_k$, the new state estimate will mostly rely on the measurements, whereas if $\boldsymbol{R}_k$ is large relative to $\bar{\boldsymbol{P}}_k$, the adjustment to the a priori state estimate will be much smaller.

The subsequent step is the measurement update,

$$\hat{x}_k = \bar{x}_k + \boldsymbol{K}_k\left(\vec{y}_k - \tilde{\boldsymbol{H}}_k \bar{x}_k\right) \tag{2.77}$$

$$\boldsymbol{P}_k = \left(\boldsymbol{I} - \boldsymbol{K}_k \tilde{\boldsymbol{H}}_k\right) \bar{\boldsymbol{P}}_k \left(\boldsymbol{I} - \boldsymbol{K}_k \tilde{\boldsymbol{H}}_k\right)^T + \boldsymbol{K}_k \boldsymbol{R} \boldsymbol{K}_k^T \tag{2.78}$$

Where $\boldsymbol{I}$ is a 6×6 identity matrix. Now the propagated state $\vec{\mathbb{X}}_k$ can be updated with the estimated state.

$$\vec{\mathbb{X}}_k = \vec{\mathbb{X}}_{\text{ref},k} + \hat{x}_k \tag{2.79}$$

With the new estimated state, new measurements can be processed and calculated until all measurement are done. For the new measurements, $\hat{x}$ has to be reset to a zero vector.

2.3.2. Unscented Estimation Techniques

In this subsection, the UBE and UKF are discussed. Both algorithms are based on the unscented transform, where the non-linear dynamics is used to estimate the state. First the unscented transform will be explained, then the unscented batch estimator (UBE) and finally the unscented Kalman filter (UKF).

Unscented Transform

The unscented transform is based on the notion that "*it is easier to approximate the probability distribution than it is to approximate an arbitrary nonlinear function or transformation*" [29]. The idea is visualised in Figure 2.8, a set of sigma-points χ are chosen with a mean $\bar{x}$ and covariance Σ. These sigma-points are then propagated with the nonlinear dynamics. The statistics of the transformed points can then be calculated to form an estimate of the nonlinearly transformed mean and covariance.

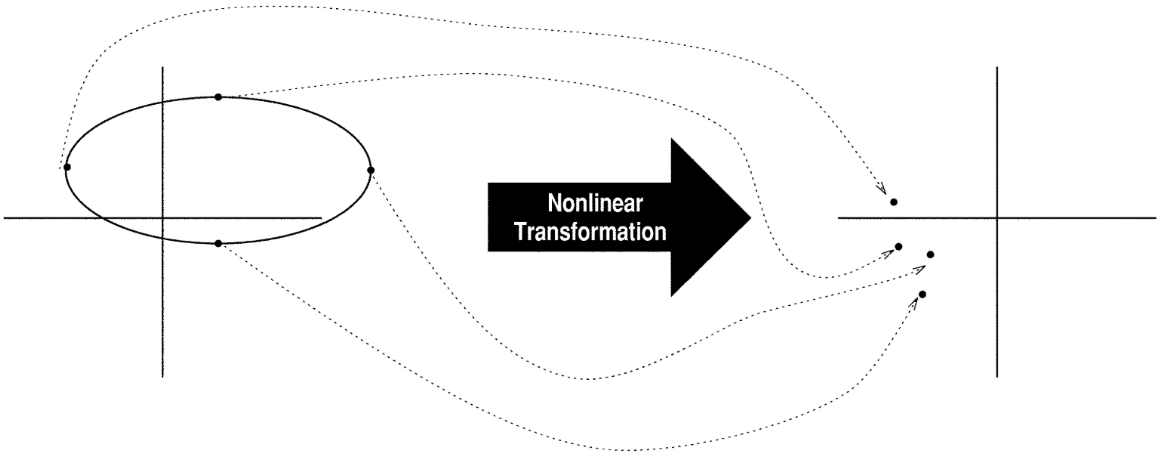

Figure 2.8: Visualisation of the unscented transform [29]

The sigma-points are chosen deterministically so that they exhibit certain specific properties (given mean and covariance). These sigma-points also have a weight to them. For an unbiased estimate, the sum of the weights must be unity.

$$\sum_{i=0}^{p} W^{(i)} = 1 \tag{2.80}$$

To calculate the sigma-points, a few coefficients have to be defined beforehand,

$$\beta = 2, \quad \alpha = 1 \times 10^{-3}, \quad \kappa = 3 - n, \tag{2.81}$$

where β incorporates knowledge about the distribution. For Gaussian distributions β is 2. α determines the spread around the mean, which typically holds a value between 1 and 1×10^{-4}, where smaller values for α cause the sigma-points to be closer to the mean. A moderate value of 1×10^{-3} is chosen for this study. With these parameters defined, the scaling factor λ can be calculated, which is defined as,

$$\lambda = \alpha^2 (n + \kappa) - n \tag{2.82}$$

where n is the number of elements in the state vector. For orbit determination $n = 6$. Finally, the weight vectors $\vec{W}_m$ and $\vec{W}_c$ can be computed before the estimation process starts.

$$W_0^m = \frac{\lambda}{n + \lambda}, \quad W_0^c = \frac{\lambda}{n + \lambda} + \left(1 - \alpha^2 + \beta\right) \tag{2.83}$$

$$W_i^m = W_i^c = \frac{1}{2(n + \lambda)}, \quad i = 1, \ldots, 2n \tag{2.84}$$

With the weights and coefficients defined, the sigma-points can be calculated based on the state and the covariance:

$$\boldsymbol{\chi}_0 = \left[\vec{\mathbb{X}}_0 \quad \vec{\mathbb{X}}_0 + \sqrt{(n+\lambda)\,\boldsymbol{P}_0} \quad \vec{\mathbb{X}}_0 - \sqrt{(n+\lambda)\,\boldsymbol{P}_0}\right] \tag{2.85}$$

The $\boldsymbol{\chi}_0$ matrix holds 13 state vectors, where the first column is the unperturbed state vector, and the other columns are perturbed based on the covariance.

Unscented Batch Estimator

The *unscented batch estimator* (UBE) is based on the work of Park et al. [38], who designed a batch estimator based on the unscented transform. It starts by defining the initial guess $\vec{\mathbb{X}}_0$ and the initial covariance $\boldsymbol{P}_0$, and the first iteration can be initialized by calculating the sigma-points based on these initial values. For later calculations, a $\delta\boldsymbol{\chi}_0$ is computed as follows,

$$\delta\boldsymbol{\chi}_0 = \boldsymbol{\chi}_0 - \vec{\mathbb{X}}_0 \tag{2.86}$$

Now the first measurement $\vec{Y}_k$ at time t_k with covariance $\boldsymbol{R}_k$ can be read, and the estimation process can start. First, the sigma-points $\boldsymbol{\chi}_0$ are propagated from time t_0 to t_k using a dynamics model. The outcome of this propagation is the new sigma-points $\boldsymbol{\chi}_{k|0}$. These sigma-points are then transformed into the measurement space using the $G()$ function. This function works in the same manner as for the conventional estimators. However, now this transformation has to be done for all state vectors. With the spacecraft state in the measurement space, the observation deviation vector can be calculated.

$$\boldsymbol{\gamma}_k = G\left(\boldsymbol{\chi}_{k|0}, t_k\right) \tag{2.87}$$

$$\bar{\gamma}_k = \sum_{i=0}^{2n} W_i^m \boldsymbol{\gamma}_{k,i} \tag{2.88}$$

$$\bar{y}_k = \vec{Y}_k - \bar{\gamma}_k \tag{2.89}$$

With all the observations processed, the state can be updated.

$$\boldsymbol{P}_{\gamma_k,\gamma_k} = \sum_{i=0}^{2n} W_i^c \left(\boldsymbol{\gamma}_{k,i} - \bar{\gamma}_k\right)\left(\boldsymbol{\gamma}_{k,i} - \bar{\gamma}_k\right)^T + \boldsymbol{R}_k \tag{2.90}$$

$$\boldsymbol{P}_{x_0,\gamma_k} = \sum_{i=0}^{2n} W_i^c \delta\boldsymbol{\chi}_{0,i} \left(\boldsymbol{\gamma}_{k,i} - \bar{\gamma}_k\right)^T \tag{2.91}$$

Now, the state deviation vector is calculated and added to the reference state. For convenience, the subscript j is introduced to indicate the iteration number.

$$(\boldsymbol{K}_k)_j = \boldsymbol{P}_{x_0,\gamma_k} \boldsymbol{P}_{\gamma_k,\gamma_k}^{-1} \tag{2.92}$$

$$(\vec{\mathbb{X}}_0)_j = (\vec{\mathbb{X}}_0)_{j-1} + (\boldsymbol{K}_k)_j \bar{y}_k \tag{2.93}$$

Now the covariance of the estimate is calculated,

$$(\boldsymbol{P}_0)_j = \left(\boldsymbol{I} - \boldsymbol{K}_k \boldsymbol{P}_{y_k,y_k} \boldsymbol{K}_k^T\right) (\boldsymbol{P}_0)_{j-1} \left(\boldsymbol{I} - \boldsymbol{K}_k \boldsymbol{P}_{y_k,y_k} \boldsymbol{K}_k^T\right)^T + \boldsymbol{K}_k \boldsymbol{R} \boldsymbol{K}_k^T \tag{2.94}$$

Finally, the algorithm will check for convergence based on the residuals in the same manner as for the batch least squares estimator. If the solution has not yet converged, a new iteration will start. Otherwise, $\vec{\mathbb{X}}_0$ will be the state estimate together with the uncertainty captured in the initial state covariance $\boldsymbol{P}_0$.

Unscented Kalman Filter

The *unscented Kalman filter* (UKF) is a sequential estimator, very similar to the EKF. It starts by defining the initial guess $\vec{\mathbb{X}}_0$ and the initial covariance $\boldsymbol{P}_0$. For the unscented transform, the same parameters can be used as shown for the unscented batch estimator. With these parameters predefined, the first measurement $\vec{Y}_k$ at time t_k with covariance $\boldsymbol{R}_k$ can be read and the estimation process can start. The first step is to calculate the sigma-points using $\mathbb{X}_{k-1}$ and $\boldsymbol{P}_{k-1}$. For the time update, these state vectors are propagated from t_{k-1} to t_k using the dynamics model $F\left(\boldsymbol{\chi}_{k-1}, t_{k-1}\right)$. The output of this propagation are the sigma-points at time t_k. The next step in the time update is,

$$\bar{x}_k = \boldsymbol{\chi}_{0,k-1} \vec{W}_m \tag{2.95}$$

$$\bar{\boldsymbol{P}}_k = \left(\boldsymbol{\chi}_{0,k-1} - \bar{x}_k\right) \vec{W}_c \left(\boldsymbol{\chi}_{0,k-1} - \bar{x}_k\right)^T + \boldsymbol{\Gamma} \boldsymbol{Q} \boldsymbol{\Gamma}^T \tag{2.96}$$

where the term $\boldsymbol{\Gamma Q \Gamma}^T$ is the *state noise compensation* (SNC). The SNC is explained with the EKF. With these intermediate $\bar{x}_k$ and $\bar{\boldsymbol{P}}_k$, a new set of sigma points can be calculated using Equation 2.85, which results in $\bar{\boldsymbol{\chi}}_k$. These new sigma-points can be transformed into the measurement space using the $G()$ function. This function works the same as the one used for the EKF.

$$\gamma_k = G\left(\bar{\boldsymbol{\chi}}_k, t_k\right) \tag{2.97}$$

$$\bar{y} = \sum_i W_{m,i} \gamma_{0,i} \tag{2.98}$$

With this established, the measurement update can be done.

$$\boldsymbol{P}_{y_k,y_k} = \left(\gamma_k - \bar{y}\right) W_c \left(\gamma_k - \bar{y}\right)^T + \boldsymbol{R}_k \tag{2.99}$$

$$\boldsymbol{P}_{x_k,y_k} = \bar{\boldsymbol{\chi}}_k W_c \left(\gamma_k - \bar{y}\right)^T \tag{2.100}$$

Then the Kalman gain can be calculated,

$$\boldsymbol{K}_k = \boldsymbol{P}_{x_k,y_k} \boldsymbol{P}_{y_k,y_k}^{-1} \tag{2.101}$$

With the Kalman gain, the estimated state $\vec{\mathbb{X}}_k$ and the corresponding covariance matrix $\boldsymbol{P}_k$ can be calculated,

$$\vec{\mathbb{X}}_k = \bar{x}_k + \boldsymbol{K}_k \left(\vec{Y}_k - \bar{y}\right) \tag{2.102}$$

$$\boldsymbol{P}_k = \left(\boldsymbol{I} - \boldsymbol{K}_k \boldsymbol{P}_{y_k,y_k} \boldsymbol{K}_k^T \bar{\boldsymbol{P}}_k^{-1}\right) \bar{\boldsymbol{P}} \left(\boldsymbol{I} - \boldsymbol{K}_k \boldsymbol{P}_{y_k,y_k} \boldsymbol{K}_k^T \bar{\boldsymbol{P}}_k^{-1}\right)^T + \boldsymbol{K}_k \boldsymbol{R}_k \boldsymbol{K}_k^T \tag{2.103}$$

where $\boldsymbol{I}$ is a 6×6 identity matrix. With this estimated state, the post-fit residuals can be calculated by using $\vec{\mathbb{X}}_k$ and $\boldsymbol{P}_k$ to compute new sigma-points. These sigma points can be fed into the $G()$ function and a new $\bar{y}_{\text{post-fit}}$ can be computed. This value can be compared to the real measurements the find the residuals. Now a new measurement can be read until all measurement have been processed.

3 Research Methodology

Research methodology is a set of systematic techniques used in research [80]. The main goal of this study is to create an overview of the performance of different IOD algorithms for radar. Subsequently, more operational questions will be addressed. A large portion of the study will be done using numerical simulations. While numerical simulations are highly informative and capable of capturing extensive details, they cannot fully replicate the complexities of real-world conditions.

Satellites in orbit are subject to a multitude of perturbations, and radar measurements inherently contain noise from various sources, including atmospheric effects. Although many of these factors can be simulated, achieving a complete replication is not feasible. Therefore, to evaluate the robustness and limitations of these algorithms, actual radar measurements will also be used. Employing real-world data is crucial not only for testing the algorithms' efficacy but also for showcasing the capabilities of the radar system. Moreover, this approach serves to validate the algorithms' performance in the operational environment. While testing with simulated data allows us to infer performance, we only truly 'know' the algorithm works as desired when it is applied to real data. It provides a crucial indicator of the current state of technology and the practical effectiveness of these algorithms in real-world applications.

To ensure the validity of these real measurements, it is imperative to select a satellite with a well-known 'true' orbit for reference. In this regard, the Sentinel-1 satellite, operated by the European Space Agency (ESA), has been chosen. Precise orbit determination data for Sentinel-1, available in three different resolutions, can be accessed via the Copernicus portal. Given that the Sentinel-1 satellite is the focal point for real measurements, it will also be employed on the numerical simulations. This ensures that comparison between numerical and real data are both meaningful and valid.

The methodology is structured as follows, first the specifications of the satellite and ground-based radar system will be discussed. Subsequently the simulation environment is described, which goes into more detail about the generation of the true trajectories and radar measurements.

3.1. Specifications of Satellite and Ground-Based Radar System

Prior to conducting any calculations or simulations, it is essential to establish and justify the specifications of the satellite and ground station. This step is crucial because numerical simulations will be benchmarked against actual measurements, necessitating the relevance and accuracy of the comparison. Using disparate satellites or radar specifications would undermine the validity of this comparison. Therefore, careful consideration of these specifications is required in advance.

3.1.1. Dummy Radar System Specifications

The present study is centred on the Thales SMART-L MM radar system, located at the Thales premises in Hengelo, the Netherlands. The introductory chapter highlights the significance of the SMART-L MM radar as one of the largest L-band phased array radars in current operation. The incorporation of *active electronically scanned array* (AESA) technology enhances its proficiency in performing multiple mission requirements, including air surveillance, ballistic missile detection and space situational awareness [52]. The installation site of the radar tower in Hengelo is illustrated in Figure 3.1. Due to the confidentiality of the performance metrics of the SMART-L MM radar, these were not available for this research. The study uses a hypothetical model radar with *space situational awareness* (SSA) capabilities comparable to the SMART-L/MM for analysis, the relative performance can be used for comparing different initial orbit determination methods, though the absolute values do not match the actual performance.

Figure 3.1: Location of the SMART-L MM radar tower in Hengelo.

The hypothetical radar design is based on publicly available data of the SMART-L MM radar and the GESTRA SSA radar, enhanced by literature insights. Information from Thales' website highlights some of the radar's capabilities. It has a maximum range of 2000 km and a minimum range of 5 km. The radar has an update time of 5 seconds, which can be shorter in staring mode, and it can track targets at zenith, which translates to a maximum elevation of 90 degrees [52]. It is also assumed that the radar has a minimum elevation of 10 degrees due to the atmospheric interference at low elevation. Verification of the radar's geographical location came from Google Maps [81], where the latitude and longitude is determined. Analysis of a photograph, showing a man next to the antenna, provided a practical approach to estimating the antenna's size. This estimation used the average height of a Dutch male, 183 cm, as a reference point, as detailed in Figure 3.2.

Figure 3.2: Dimensional assessment of the SMART-L MM radar antenna using a human reference [82]. The antenna measures 8.34 meters in width and 2.84 meters in height, totalling an area of 23.7 m^2.

To refine the parameters for the hypothetical radar, the study uses the *German Experimental Surveillance and Tracking Radar* (GESTRA) as a reference. GESTRA operates in the L-band, similar to the SMART-L MM, which has a frequency range of 1 to 2 GHz. For this hypothetical radar, a median frequency of 1.5 GHz is chosen. In comparison, GESTRA can function at bandwidths of either 2 MHz or 10 MHz. This study opts for the lower 2 MHz bandwidth for a more conservative approach [83]. With the frequency and aperture size defined, an estimate on the radar beamwidth in azimuth and elevation can be made using the following equations [58],

$$BW_\phi = \frac{70\lambda}{W} = 1.67°, \quad BW_\theta = \frac{70\lambda}{H} = 4.92° \tag{3.1}$$

Skolnik's research indicates that pulse radars have a duty cycle ranging from 0.001 to 0.5.

Aligning with this, a mean value of 0.25 is selected for our radar's duty cycle [59]. The GESTRA radar, with a pulse repetition time (PRT) of 40 ms and a maximum pulse duration of 8.5 ms, has a duty cycle of 0.2125. This value is in close agreement with the 0.25 figure adopted for the dummy radar. Additionally, GESTRA's setup includes 256 antenna elements, each rated at 1000 watts, leading to a total power of 256 kW. It is also assumed that the radar system operates at a standard room temperature of 290 K.

For analytical purposes, it is hypothesised that the radar possesses a 50% likelihood of detecting a 1 m^2 radar cross-section object at a distance of 2000 km, aligning with a study on the performance assessment for SSA sensors [84]. This detection probability also rationalises the dummy radar's adoption of the SMART-L MM's maximum instrumented range of 2000 km. The *receiver operating characteristic* (ROC) curve facilitates the determination of the threshold signal-to-noise ratio for a 50% detection probability. The derivation of this ROC curve will be explained in the next paragraph. From Figure 3.3, this ratio is determined to be 10.9 dB. Setting this benchmark allows for the calibration of the radar's performance budget to match anticipated outcomes. The radar equation is formulated to accommodate for system losses. For example, there is some loss in the signal level as it travels from the transmitter to the antenna, through a waveguide or coaxial cable, and through devices such as a circulator, directional coupler, or transmit/receive (T/R) switch. Not only the system itself causes signal losses, the environment and atmosphere also cause such losses. These losses impact the detection capability by reducing the signal-to-noise ratio, but do not affect measurement accuracy. By adjusting the system losses, the radar budget can be changed such that it gets the right signal-to-noise ratio for the 50% detectibility at 2000 km range.

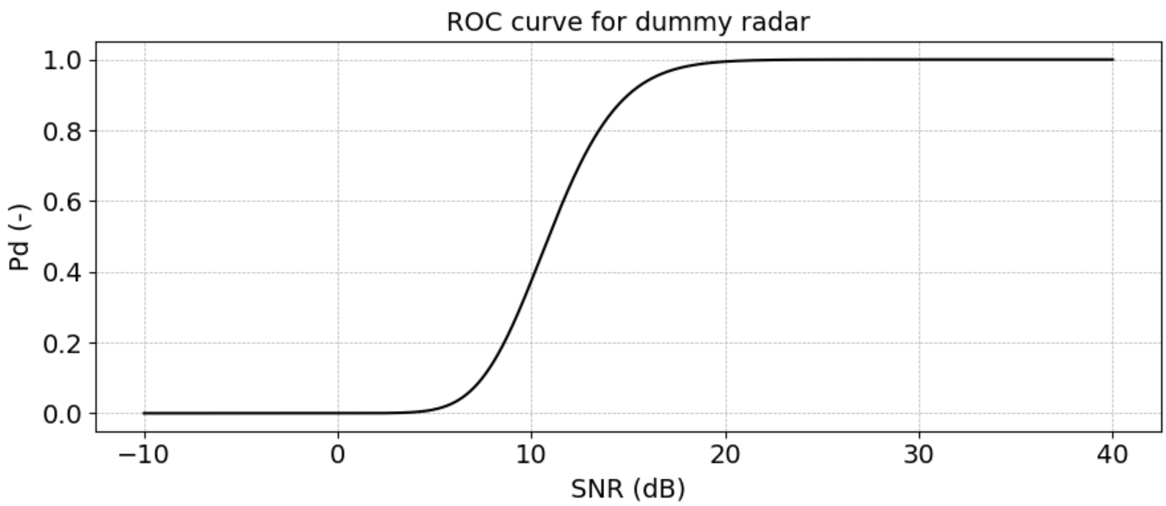

Figure 3.3: ROC curve illustrating the detection probability as a function of SNR, for a target assuming the Swerling Case 1 model and a 3-out-of-5 detection criterion with $P_{fa} = 1 \times 10^{-4}$ and assuming that the target has an RCS of 1 m^2.

The ROC-curve depicted in Figure 3.3 requires further elaboration. It is constructed by initially setting the detection threshold for each SNR value, which is based on the χ^2-distribution, considering a specific probability of false alarm (P_{fa}) and Swerling case scenario. For this research, a P_{fa} of 1×10^{-4} is selected along with a Swerling Case 1 target, which will be detailed in 3.1.2. This process computes the SNR required for the detection of a single pulse to exceed the set threshold, maintaining the defined probability of a false alarm.

Detection decisions are often based on more than one detection pulse due to considerations of noise and target fluctuations [59]. A common criterion used is the M-out-of-N rule, which requires that at least M pulses out of N transmitted pulses exceed the detection threshold. For this study, a 3-out-of-5 detection criteria is used. This value is based on a trade-off between a high false alarm rate and a low detection rate. If one would impose a 1-out-of 5 detection criteria, a single noise fluctuation would be considered a detection. But for a 4-out-of-5 detection criteria, almost every received pulse would have to surpass the detection threshold, and due to RCS fluctuations, this might be impossible. This will result in a low detection rate. It is a rather complex engineering trade-off as one wants to maximise the detection rate and minimise the number of false alarms. Skolnik suggests either a 2-out-of-3, 3-out-of-4 or 3-out-of-5 detection criteria [59]. Hence, a moderate value of 3-out-of-5 is chosen as a detection criterion. The 3-out-of-5 detection criterion utilises a combinatorial approach to calculate the probability that at least three out of the five pulses surpass the detection threshold, applying a binomial distribution. For each SNR value, this probability is calculated by summing the probabilities of all scenarios where three or more pulses meet or exceed the SNR threshold, alongside the probabilities of the remaining pulses falling below the threshold, thus defining the detection probability for each SNR value.

Next, the determination of the Pulse Repetition Time (PRT) is based on the radar's maximum instrumented range. It is computed using the equation:

$$PRT = \frac{2R_{\text{max}}}{c} = 0.0134 \text{ s} = 13.4 \text{ ms} \tag{3.2}$$

where R_{max} represents the maximum range, and c denotes the speed of light. This calculation yields a PRT of 13.4 milliseconds. Subsequently, the pulse duration is obtained considering the radar's duty cycle, set at 0.25. The formula used is:

$$DC = \frac{\tau}{PRT} \rightarrow \tau = DC \cdot PRT = 0.0033 \text{ s}, = 3.3 \text{ ms} \tag{3.3}$$

where τ signifies the pulse duration, revealing a duration of 3.3 milliseconds. With this information the system losses can be determined. First the radar equation is restated,

$$SNR = \frac{P_t \tau G_t A_e \left(RCS\right)}{\left(4\pi\right)^2 k T_s R^4 L_i} \tag{3.4}$$

Using the predetermined signal-to-noise ratio threshold of $10.9dB$, the system losses can be determined,

$$L_i = \frac{P_t \tau G_t A_e \left(RCS\right)}{\left(4\pi\right)^2 k T_s R^4 \left(SNR_{\text{threshold}}\right)} = 0.75 \text{ dB} \tag{3.5}$$

The radar parameters for the hypothetical radar are summarised in Table 3.1.

Table 3.1: Parameters for the hypothetical dummy radar

Parameter	Specification	Source
Latitude, ϕ_{gs} (deg)	52.2470366	[81]
Longitude, λ_{gs} (deg)	6.7695056	[81]
Altitude, h_{gs} (m)	100	[81]
Frequency band	L-band	[52]
Instrumented range, R (km)	[5, 2000]	[52]
Maximum elevation, θ_{max} (deg)	90	[52]
Minimum elevation, θ_{min} (deg)	10	-
Update time, t_{up} (s)	5	[52]
Effective aperture, A_e (m^2)	23.7	Figure 3.2, [82]
Beamwidth azimuth, BW_ϕ (deg)	1.67	-
Beamwidth elevation, BW_θ (deg)	4.92	-
Frequency, f (GHz)	1.5	-
Bandwidth, B (MHz)	2.0	[83]
Transmit power, P_t (kW)	256	[85]
System losses, L_i (dB)	0.75	-
System temperature, T_s (K)	290	-
Duty cycle, DC	0.25	[59]
Pulse repetition time, PRT (ms)	13.3	-
Pulse length, τ (ms)	3.3	-
Radar budget, C (dB)	263.00	-

3.1.2. Sentinel-1A Satellite Specifications

Launched by the *European Space Agency* (ESA) in 2014, the Sentinel-1 mission forms part of the Copernicus Earth observation program. This mission consists of a constellation of two identical satellites, Sentinel-1A and Sentinel-1B. Sentinel-1A, was launched on April 3rd, 2014 from Kourou in French Guiana and an artists impression of the satellite can be seen in Figure 3.4. Its main mission is monitoring the Earth's landmasses and oceans, in addition to providing data for emergency response initiatives, using its *Synthetic Aperture Radar* (SAR).

The selection of Sentinel-1A as the primary focus of this study is attributed to the availability of precise orbit determination data from ESA. This data is accessible in three distinct resolutions through the Copernicus portal, detailed in Table 3.2. Because both numerical simulations are done, and real measurements will be used, it is important that for both scenarios, the same satellite is used. This makes sure that the comparison between the numerical simulations and real data are both meaningful and valid.

Table 3.2: The timeliness and performance results of the precise orbital product provided by ESA [86].

Category	Latency	Orbit Accuracy
NRT Predicted (AUX_PREORB)	30 minutes	1 m (2D RMS 1σ)
NRT (AUX_RESORB)	180 minutes	10 cm (2D RMS 1σ)
NTC (AUX_POEORB)	20 days	5 cm (3D RMS 1σ)

Figure 3.4: Artist impression of the Sentinel-1 satellite [87].

From the geometry of the Sentinel-1 satellites in Figure 3.5, it is possible to not only establish a reference area of 6.2 m^2 and a length of 19.264 m, but also to determine the appropriate Swerling case for modelling the radar cross-section (RCS). The Swerling Case 1 is considered most suitable for describing the Sentinel-1 satellites because they feature two large, identical solar panels which act as the primary reflectors. Given that the satellite maintains a stable flight path without tumbling, it is assumed that the RCS will exhibit only slow changes over time, akin to an aircraft in cruise flight.

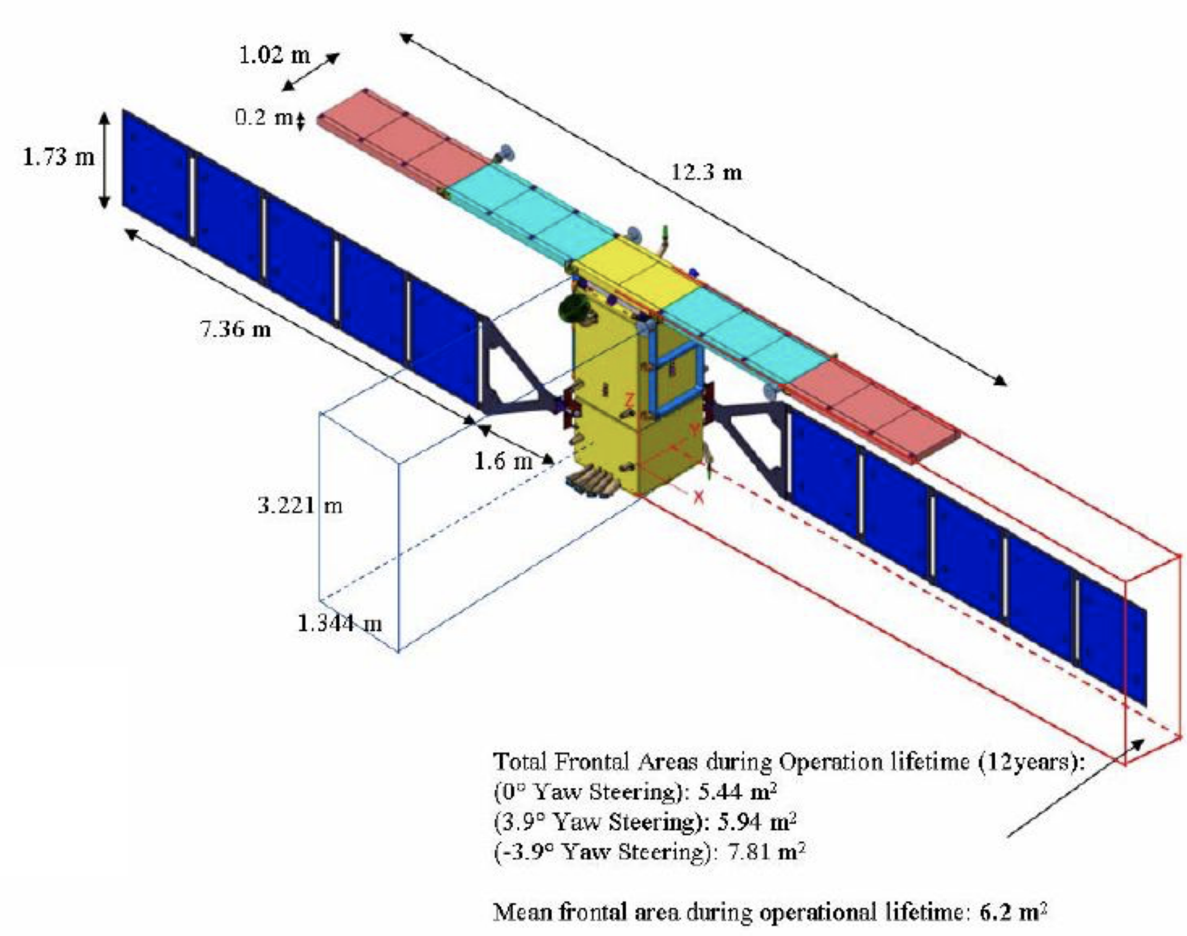

Figure 3.5: Geometry of the Sentinel-1 satellites [88]

From the Copernicus portal, relevant parameters and specification can be acquired, these are summarised in Table 3.3.

Table 3.3: Specifications of the Sentinel-1A Satellite [89]. Asterisks denote assumed values.

Parameter	Specification	Source
NORAD ID	39634	[90]
Launch date	April 3, 2014	-
Launch site	French Guiana, Kourou	-
Perigee (km)	695	[90]
Apogee (km)	697	[90]
Cross section, A (m^2)	6.2	[88]
Length, L (m)	19.264	[88]
Drag coefficient, C_D (-)	2.2*	-
Reflectivity, C_R (-)	1*	-
Mass, m (kg)	2133.730	[91]
Radar cross section, RCS (m^2)	1*	-
Swerling case	SW1	-

To get the initial state of Sentinel-1A, TLE data is used. The TLE strings can be converted to the initial state by orekit's TLE propagator. A TLE string can be seen in Table 3.4.

Table 3.4: Sentinel-1A TLE, accessed on February 20th 2024.

```
Sentinel-1A
1 39634U 14016A   24051.13915294  .00000502  00000+0  11617-3 0  9998
2 39634  98.1824  59.9272 0001319  91.0874 269.0477 14.59200160526372
```

3.2. Simulation Environment

To address the research questions, this study uses numerical simulations in Python to generate simulated radar measurements of the object in orbit, subsequently applying the Initial Orbit Determination (IOD) algorithms. The primary tool used is Orekit's Python wrapper [92]. Orekit is a low level, space dynamics library used by internationally recognised research institutes and organisations such as Airbus Defence and Space, Thales Alenia Space and the U.S. Naval Research Laboratory [92]. By comparing the numerically derived true trajectory with the estimated trajectory, the root mean square error (RMSE) can be computed.

3.2.1. Generating Truth Trajectory

The generation of truth trajectories using Orekit's Python wrapper [92] takes into account various forces acting on the spacecraft to simulate a realistic trajectory. These forces include:

- Earth's gravitational force: Modelled using spherical harmonics up to order 10 and degree 10, accounting for Earth's non-uniform mass distribution.
- Third body perturbations: The gravitational influence of the Sun, Moon, Jupiter, Saturn, and Mars is calculated, considering these bodies as point masses.
- Atmospheric drag: The NRLMSISE-00 atmospheric model simulates the drag exerted by Earth's atmosphere on the spacecraft, for which a spherical shape model is assumed.
- Solar-radiation pressure: Simulates the force exerted by solar radiation on the spacecraft, for which a spherical shape model is assumed.

3.2.2. Generating Radar Measurements

Orekit has a measurement sub-package to generate and process measurements. With the use of this sub-package, range, azimuth, elevation and radial velocity measurements are generated from the ground station. An example of these measurements can be seen in Figure 3.6, using the TLE from 3.4. The measurements from Figure 3.6 are essentially the spacecraft state converted to measurements space including the light time delay. However, it does not check whether the spacecraft is within the radar's operational constraints, or include any errors.

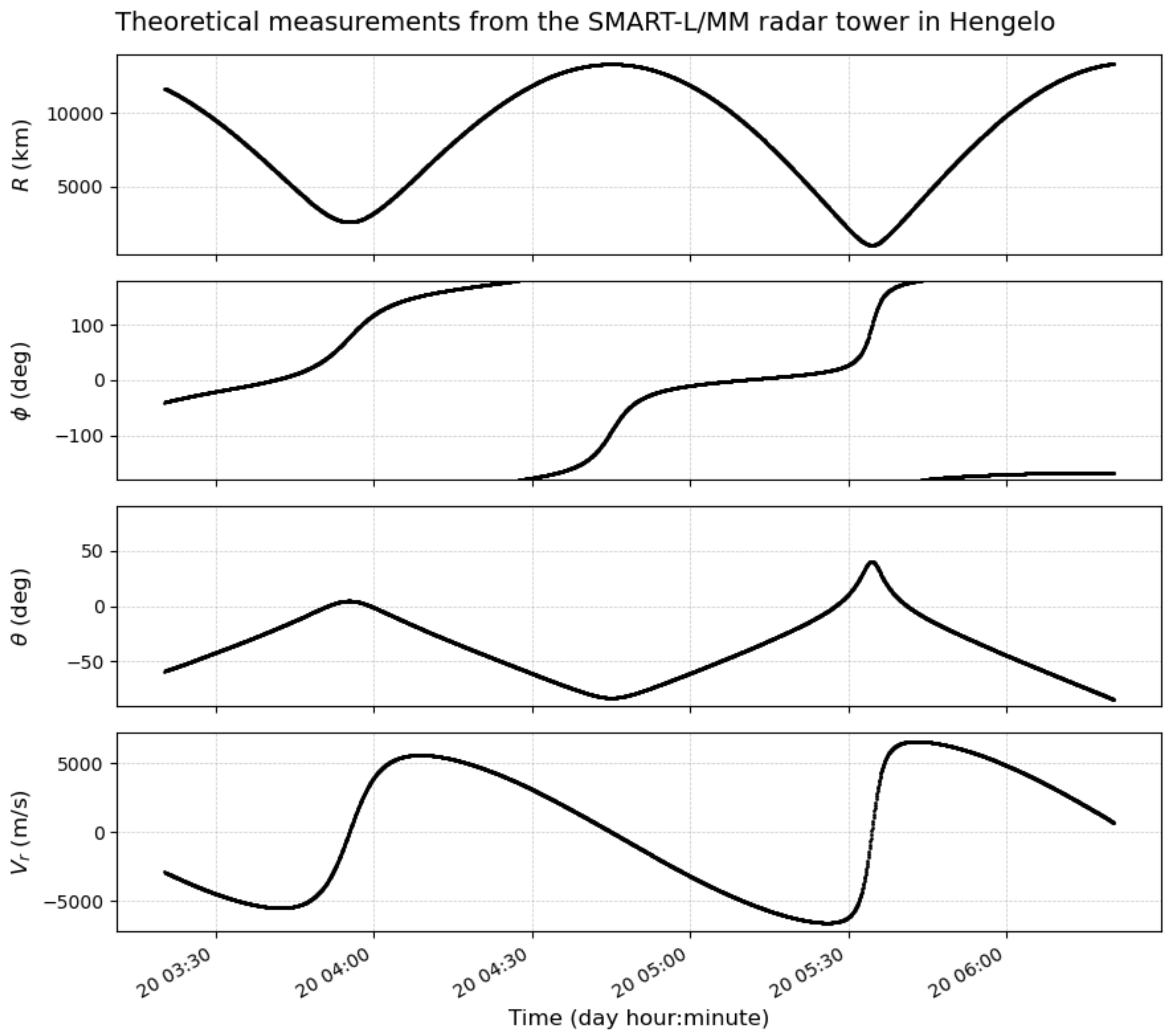

Figure 3.6: Example of theoretical measurements using the TLE data from Table 3.4. The measurements comprise of the range R, azimuth ϕ, elevation θ and radial velocity V_r.

With these theoretical radar measurements in hand, further processing steps are implemented to enhance the realism of these measurements. This involves adding noise to the data and filtering out measurements that fall outside the radar's operational constraints.

The first step is to determine the signal-to-noise ratio of the measurement. Using the range measurements alongside the radar and satellite parameters from Table 3.1 and Table 3.3, the SNR can be calculated using the radar equation.

$$SNR = C\frac{RCS}{R^4} \tag{3.6}$$

Using the ROC curve from Figure 3.3, the probability of detection (P_d), can be determined. A random number, Z, drawn from a uniform distribution $\mathcal{U}\,[0,1]$, is then compared with P_d to decide if a measurement is detected or not:

$$\text{Detection} = \begin{cases} \text{True} & \text{if } Z \leq P_d \\ \text{False} & \text{otherwise} \end{cases}, \text{ where } Z \sim \mathcal{U}\,[0,1] \tag{3.7}$$

Subsequently, noise is introduced as error. The standard deviation of this noise error is calculated based on the SNR, and the glint error for range is determined according to the spacecraft's size, as shown in Figure 3.7.

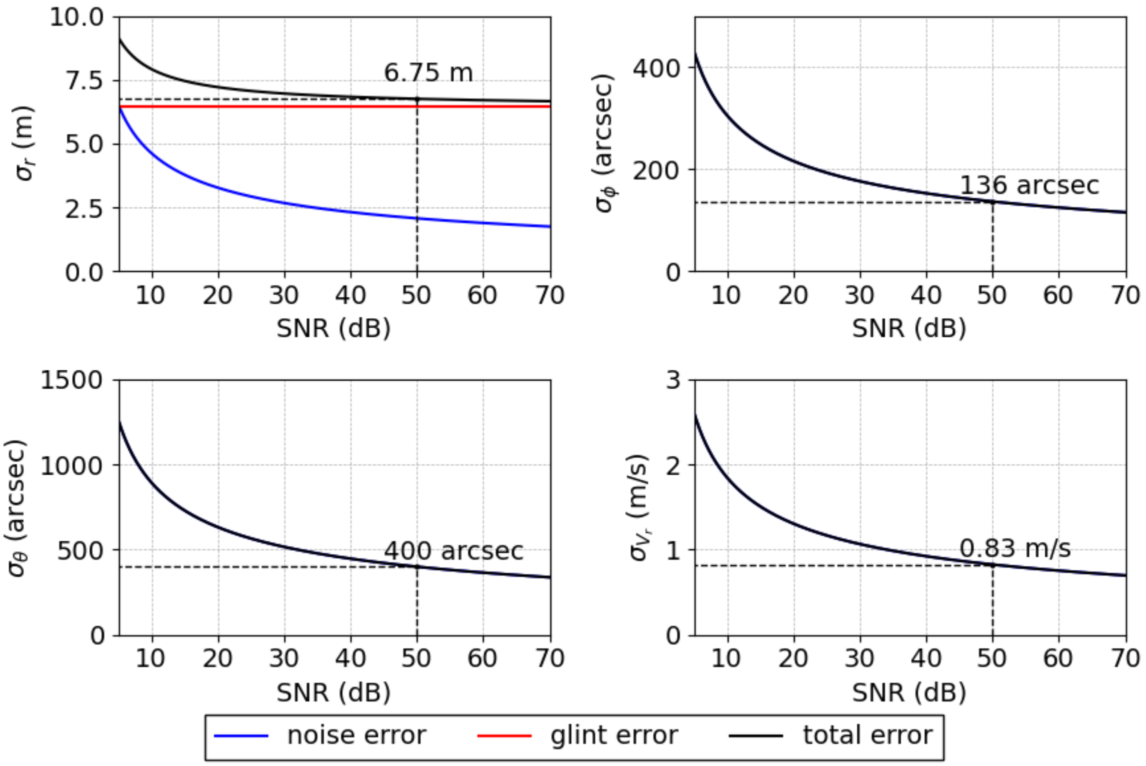

Figure 3.7: The standard deviation for all four radar coordinates with its subcomponents. Blue indicates the noise error, red indicates the glint error (only for range) and black indicates the total error. The numbers indicate the value at the 50 dB threshold

A simplified approach calculates the instrument error, which is considered the radar accuracy's lower bound. By combining noise and glint errors, a $\sigma_{\text{noise+glint}} - SNR$ curve is generated for all four measurements. This is achieved by summing the covariances and taking the square root, as shown in Figure 3.7. The instrument error is established by reading off the standard deviation of the total error at a certain threshold. For this study, the threshold is set at 50 dB SNR. It is assumed that the system cannot improve in performance after a 50 dB SNR. The final standard deviation curves are computed by combining the noise, glint, and instrument errors,

$$\sigma_{\text{total}} = \sqrt{\sigma^2_{\text{noise}} + \sigma^2_{\text{glint}} + \sigma^2_{\text{instrument}}} \tag{3.8}$$

The result is depicted in Figure 3.8.

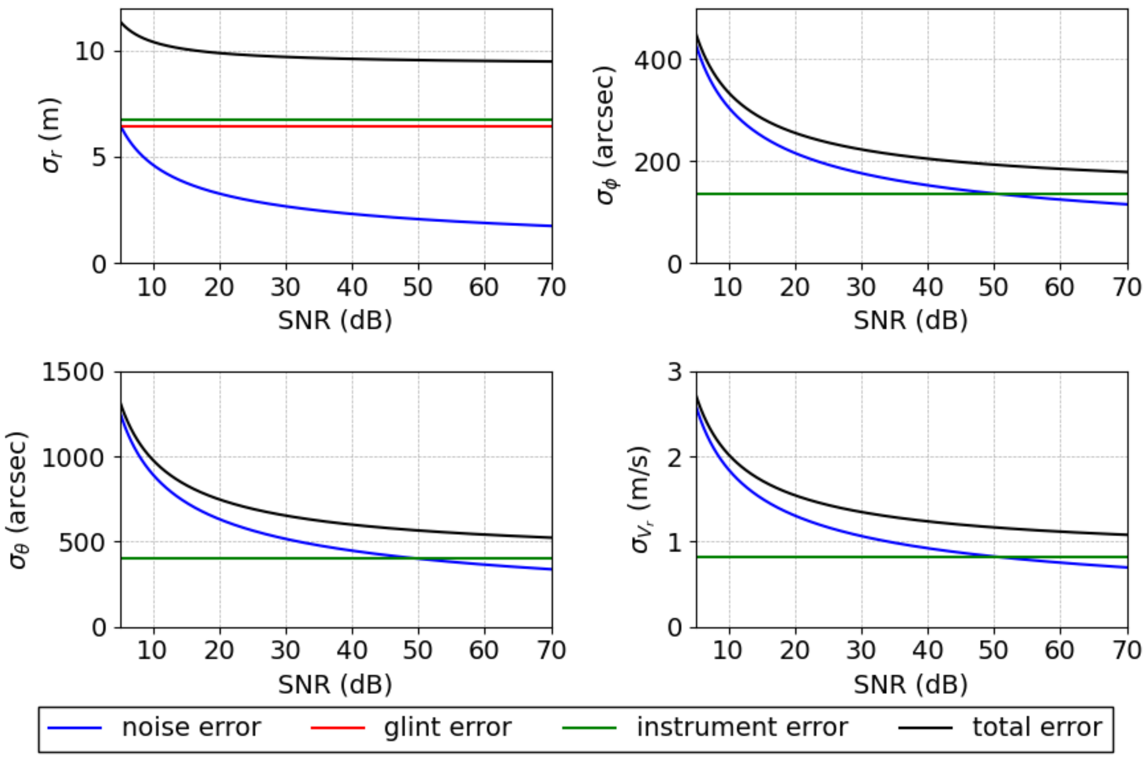

Figure 3.8: The standard deviation for all four radar coordinates with its subcomponents. Blue indicates the noise error, red indicates the glint error (only for range), green indicates the instrument error and black indicates the total error

Noise is then added to the measurements as follows,

$$\begin{bmatrix} R_n \\ \phi_n \\ \theta_n \\ V_{R,n} \end{bmatrix} = \begin{bmatrix} \mathcal{N}\left[R_c, \sigma_r\right] \\ \mathcal{N}\left[\phi_c, \sigma_\phi\right] \\ \mathcal{N}\left[\theta_c, \sigma_\theta\right] \\ \mathcal{N}\left[V_{R,c}, \sigma_{V_r}\right] \end{bmatrix} \tag{3.9}$$

where subscript n indicates noisy parameters and subscript c clean parameters. The measurements are finally compared to the radar's operational constraints. The radar's design specifies a maximum effective range of 2000 km and incorporates a pulse length of 500 km. As a result, the radar is incapable of receiving signals from 0 to 500 km due to the transmission of a pulse, and similarly, signals from 2000 to 2500 km are beyond its reception capability for the same reason. Additionally, the radar operates within specified elevation angles, from 10° to 90°. These constraints dictate the final criterion for determining the validity of measurements, ensuring they fall within the radar's designed operational parameters.

$$\text{Valid measurements} = \begin{cases} \text{True} & \text{if } 500 \leq R \leq 2000 \text{ km and } 10° \leq \theta \leq 90° \\ \text{False} & \text{otherwise} \end{cases} \tag{3.10}$$

An example of these measurements can be seen in Figure 3.9. From this figure it can be observed that the measurements are most accurate near zenith. At this point, the range to the spacecraft is the minimum, thus the signal-to-noise ratio is maximum.

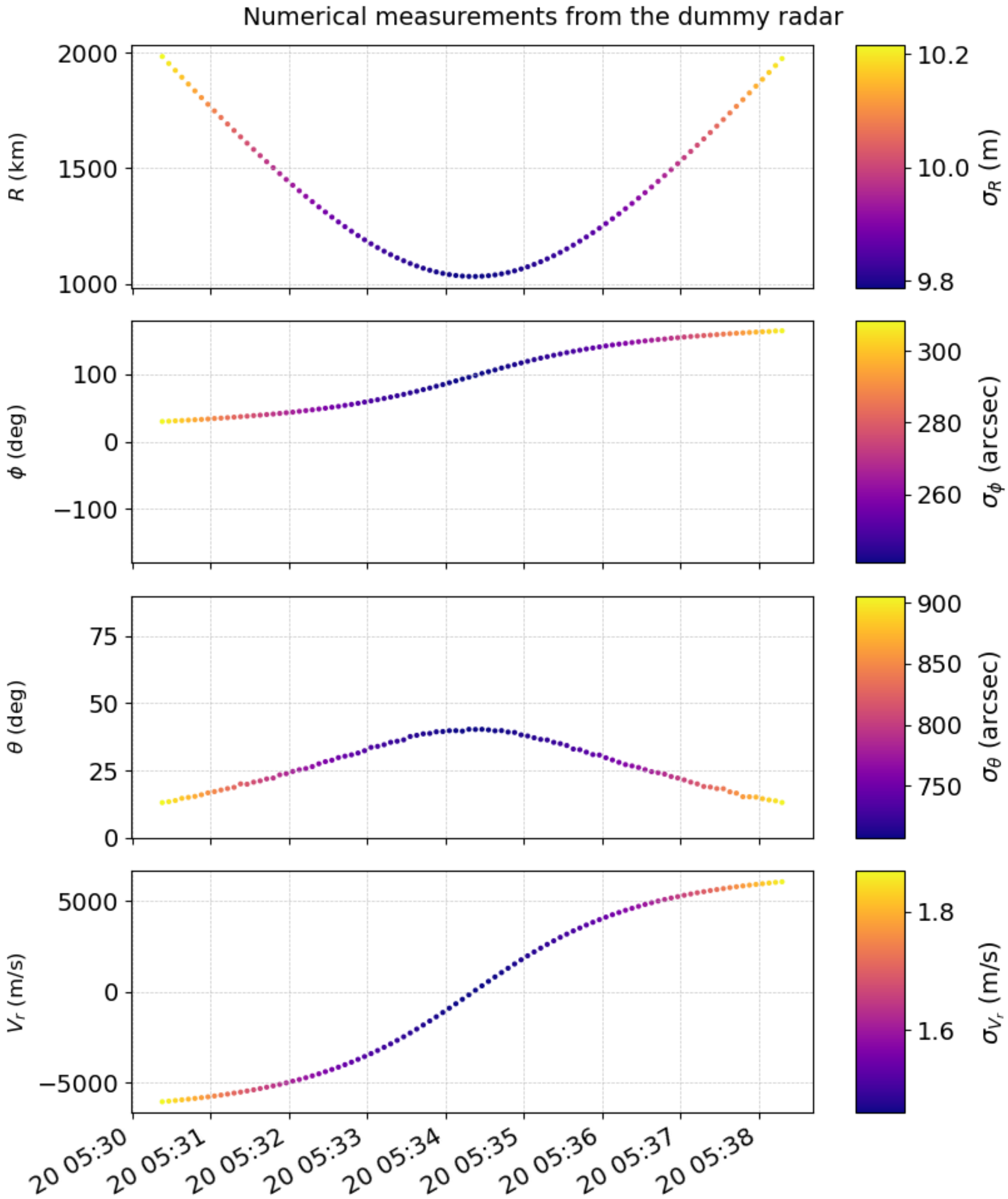

Figure 3.9: Example of realistic measurements using the TLE data from Table 3.4. The measurements comprise of the range R, azimuth ϕ, elevation θ and radial velocity V_r. The colour bars indicate the standard deviation of the measurements.

3.3. Real Radar Data Integration

The specifications of the SMART-L MM radar and the measurements are confidential. The research questions will be answered using the dummy radar and real radar measurements and their results will be compared. The methodology and results are not available for general public. However, the conclusions will be shared in the main report.

4

Performance Comparison of IOD Algorithms with Radar Data

This chapter evaluates the performance of the four different IOD algorithms using simulated radar data, and real radar measurements. The main focus is on the RMSE of the estimated state, and the position error over time.

4.1. Methodology

The methodology involves generating a truth trajectory and corresponding measurements. An initial guess is made using a Lambert targeting algorithm, which calculates the spacecraft state at the first epoch based on two position vectors and the flight time between them. These position vectors are derived from range, azimuth, and elevation measurements.

The state of the spacecraft is estimated using the following four algorithms,

1. Batch least squares estimator (BLSE)
2. Extended Kalman filter (EKF)
3. Unscented Kalman filter (UKF)
4. Unscented batch estimator (UBE)

The batch estimators estimate the initial state of the trajectory, which is then propagated over time to create a full trajectory. Sequential estimators, on the other hand, estimate the state continuously as new measurements are processed. Due to the need for sequential estimators to converge over time, the RMSE of the position is calculated from the second half of the estimated trajectory, where a steady state is assumed.

$$\text{RMSE} = \sqrt{\frac{1}{m}\sum_{k=0}^{m}\left(\vec{r}_{\text{true},k} - \vec{r}_{\text{est},k}\right)^2} \tag{4.1}$$

where m is the number of measurements, $\vec{r}_{\text{true},k}$ is the true position at time k and $\vec{r}_{\text{est},k}$ is the estimated position at time k. The RMSE provides a single value as a performance measure for the full trajectory. The time evolution of the error is also analysed using:

$$\varepsilon_r(t) = ||\vec{r}_{\text{true}}(t) - \vec{r}_{\text{est}}(t)|| \tag{4.2}$$

Robustness of the algorithms is evaluated by varying the initial guess and calculating the RMSE across 100 Monte Carlo runs. These runs involve perturbing the true state with a random sample from the initial covariance matrix $\boldsymbol{P}_0$. A standard deviation of 25 km is chosen for the position, and 25 m/s for the velocity.

$$\vec{\mathbb{X}}_{\text{perturbed}} = \mathcal{N}\left[\vec{\mathbb{X}}_{\text{true}}, \boldsymbol{P}_0\right] \tag{4.3}$$

For the simulation, the Sentinel-1A satellite trajectory is used. TLE data is converted to a Cartesian state, which is subsequently propagated in time using the predefined dynamics model (Table 3.4). A comparison of the initial guess with the reference state shows differences in position and velocity components, as detailed in Table 1.

Table 4.1: Initial guess using the Lambert targetting algorithm.

	r_x (m)	r_y (m)	r_z (m)	v_x (m/s)	v_y (m/s)	v_z (m/s)
Truth	-630805.00	-2930406.31	6399490.86	-3845.15	-5715.48	-2989.68
Init guess	-638778.85	-2948390.24	6393713.49	-3829.06	-5699.92	-3015.18
Diff (abs)	7973.85	17983.93	5777.37	16.09	15.56	25.51
Diff (%)	1.26	0.61	-0.09	-0.42	-0.27	0.85

4.2. Results Simulated Data

The differences in position and velocity between the estimated state and the true state over time are shown in Figure 4.1, with different colours representing the four estimation algorithms.

The BLSE, indicated in black converged after 5 iterations. It shows a smooth and stable curve over time with an RMSE of 717.78 meters. The EKF, indicated in red, starts with a large deviation, but as time progresses it converges to a steady state of roughly 1600 meters resulting in an RMSE of 1727.72 meters. There is also a large dip in the position error after roughly 75 seconds, but this dip is only for a short time before further deviating from the true state. A noticeable difference between the BLSE and the EKF is that the estimated state of the EKF is less smooth. This is due to the nature of the estimators. The BLSE estimates the initial state, which is subsequently propagated forward resulting in a smooth curve. The EKF however, updates the estimated state each time a measurement is processed, producing a discontinuous trajectory.

The UKF. indicated in blue, shows a similar behaviour as the EKF. At the end of the trajectory, the steady state reaches a smaller error than the EKF around 500 meters, with an RMSE of 670.61 meters. Finally, the UBE, indicated in green, converged after 4 iterations. It shows a similar behaviour as the BLSE, however the error is smaller with a RMSE of 606.34 meters, showing the best average performance of all the tested algorithms for the Sentinel-1A overflight. The RMSE values and iteration counts for each estimation technique are summarised in Table 4.2, highlighting that the UBE has the lowest RMSE and fastest convergence.

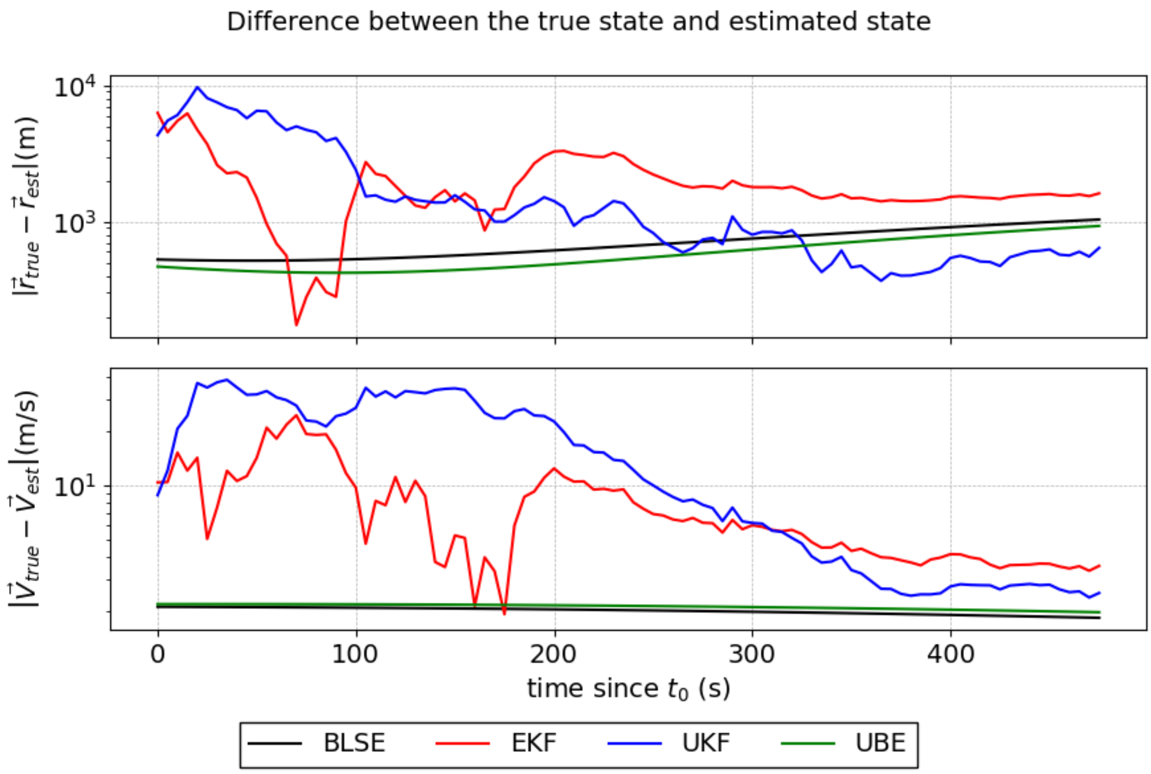

Figure 4.1: Difference in position (top) and velocity (bottom) between the estimated state and the true trajectory for the Sentinel-1A satellite using the four different estimation techniques.

From Figure 4.1, another observation can be made. The batch estimators perform better than the sequential estimators in their respective categories (conventional linearisation and unscented transform). This is to be expected as the batch estimators iterate multiple times over the measurements until the convergence threshold is reached. The sequential estimators do not use this mechanic. This is also the reason why both batch estimators have a similar estimated state, as they solve for the same convergence criteria. Yet, the BLSE converged after 5 iterations whereas the UBE converged after 4 iterations, which indicates that the UBE performs better, as it converges slightly faster.

In Figure 4.2, the results from 100 Monte-Carlo runs are depicted, showing the RMSE for each run. From the figure, it can be seen that the BLSE and UBE demonstrate consistent convergence behaviour, with convergence largely independent of the initial conditions. This is because the batch estimators iterate over the full set of measurements until the convergence criteria is met, which results in a global optimisation. Despite the use of identical convergence criteria, the UBE achieves a lower average RMSE compared to the BLSE. While the linearization in the BLSE may contribute to some estimation inaccuracies, it is more appropriate to highlight that the UBE provides a more comprehensive representation of nonlinear systems and estimation.

The sequential estimators however, exhibit significant fluctuations, indicating a higher sensitivity to the initial guess of the estimator. This sensitivity is due to the sequential nature of these estimators, where each update depends on the previous state estimate, leading to error propagation if the initial guess is not accurate. Although the RMSE of the EKF and UKF fluctuate, the UKF has a lower mean RMSE value than the mean RMSE of the EKF. Occasionally, the RMSE of the UKF is even lower than both the BLSE and UBE. This can be attributed to the UKF's ability to dynamically update its state estimates in real-time, allowing it to adapt more effectively to changing system dynamics and measurement conditions. The averaged RMSE values for the four estimation methods are summarised in Table 4.2, highlighting that the UBE has the lowest mean RMSE and the fastest convergence.

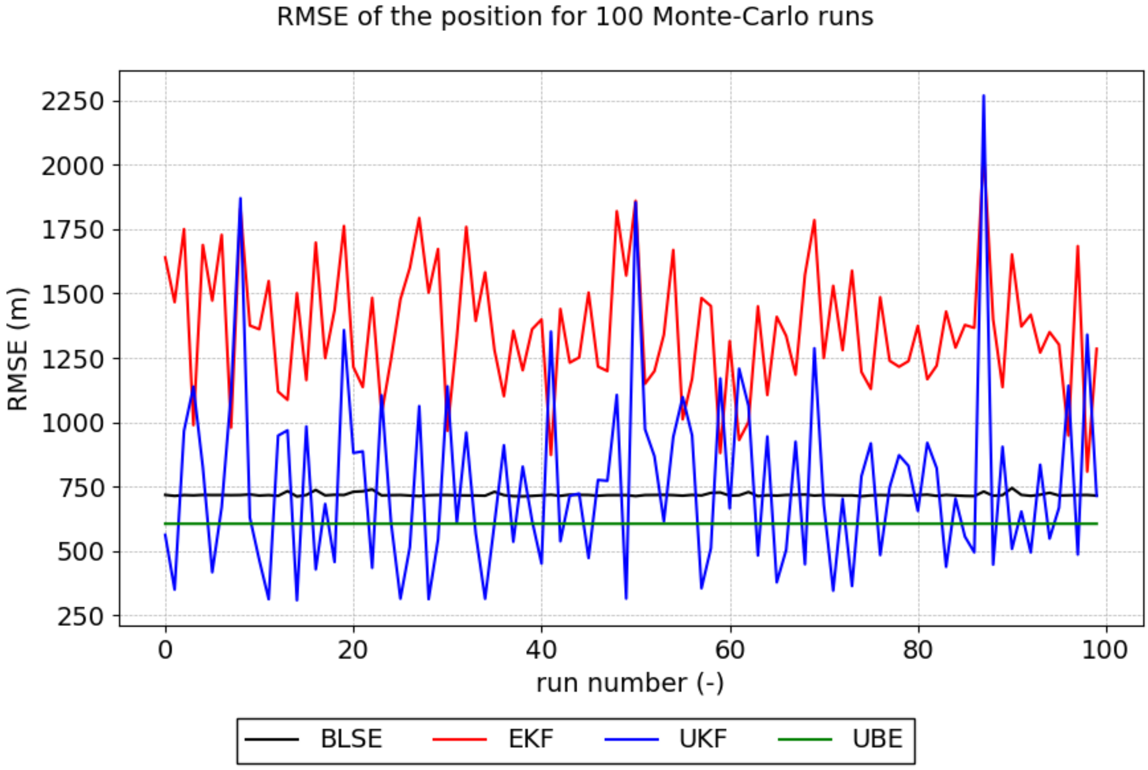

Figure 4.2: RMSE for 100 Monte-Carlo runs.

Table 4.2: Comparison of estimation techniques for a single run (top) and averaged results from 100 Monte Carlo simulations (bottom)

Single Run Data		
Estimation Method	RMSE (m)	Iterations
BLSE	717.78	5
EKF	1727.72	-
UKF	670.61	-
UBE	606.34	4
100 Monte-Carlo Runs (mean)		
Estimation Method	RMSE (m)	Iterations
BLSE	718.51	6
EKF	1361.92	-
UKF	760.52	-
UBE	606.33	4

The unscented batch estimator (UBE) is identified as the best performer for the simulated data set. It demonstrated the lowest mean RMSE among the estimators, converged more quickly, and showed significant robustness against varying initial conditions.

4.3. Results Real Radar Data

The methodology was also applied to real radar data, yielding results that differ from those obtained with simulated data. In the single runs using real radar data, the order of RMSE performance for the algorithms changes. The best performing algorithm is the BLSE, followed by the UBE, then the EKF, and finally the UKF. The difference in RMSE between the BLSE and UBE is approximately 1.5%, and between the EKF and UKF, it is roughly 2%. In contrast, for the simulated data, the performance differences are more pronounced, with the batch estimators showing a 15.5% difference and the sequential estimators a 61.2% difference.

Given the closeness in performance of the two batch estimators, the relative difference between the batch and sequential estimators is approximately 33%. This highlights that while the batch estimators (BLSE and UBE) perform similarly to each other and better than the sequential estimators in real-world scenarios, the performance gap between the sequential estimators (EKF and UKF) remains smaller. The real data results suggest a narrower margin of superiority for the batch methods compared to what was observed with the simulated data, emphasising the need for context-specific evaluations of algorithm performance.

The same methodology for the 100 Monte-Carlo runs was applied for the real measurements, where the initial guess was computed by perturbing the true state with a random sample from the initial covariance matrix $\boldsymbol{P}_0$. For the 100 Monte-Carlo runs, similar results as for a single run can be seen, where the BLSE performs better than the UBE, and the EKF performs better than the UKF. The average RMSE of the estimators are within the same order of magnitude as for the single run. However, the sequential estimators don't fluctuate as much as for the simulated data, indicating more stability.

This result however is not in line with the expectation, and they differ from the simulated data. It is expected that the algorithms utilising the unscented transform would outperform the algorithms with the conventional linearisation. There are two mayor effects that are not considered in the simulations. The first one being the atmospheric interference, which causes a non-constant bias on the range measurements. The second is the assumption of non-correlated Gaussian noise.

All the algorithms assume non-correlated Gaussian noise in the measurements. This assumption generally holds for the simulated data but may not be valid for real radar data. Real-world measurements often have correlated noise and non-Gaussian characteristics due to multipath effects, sensor imperfections, and environmental factors. These deviations from the idealised assumptions can impact all algorithms, but the degree of impact varies based on the algorithm's design and sensitivity to these factors.

The unscented transform has tuning parameters to fine tune the output. One of the tuning parameters is the noise characteristic, β. For Gaussian distributed measurements, a value of $\beta = 2$ is assumed, however, it could be that the parameters do not align with the measurements which causes this discrepancy. The tuning of these parameters could be a considered a topic for future research to improve estimator performance with real data.

4.4. Simulated UBE Estimation Results

The unscented batch estimator (UBE) demonstrates the best performance for the simulated data, and its output is detailed in this section. Figure 4.3 shows the post-fit residuals for range, azimuth, elevation, and radial velocity, with $\pm 2\sigma$ bounds indicated in red. Ideally, the residuals should appear as random noise within these bounds, indicating proper estimator performance.

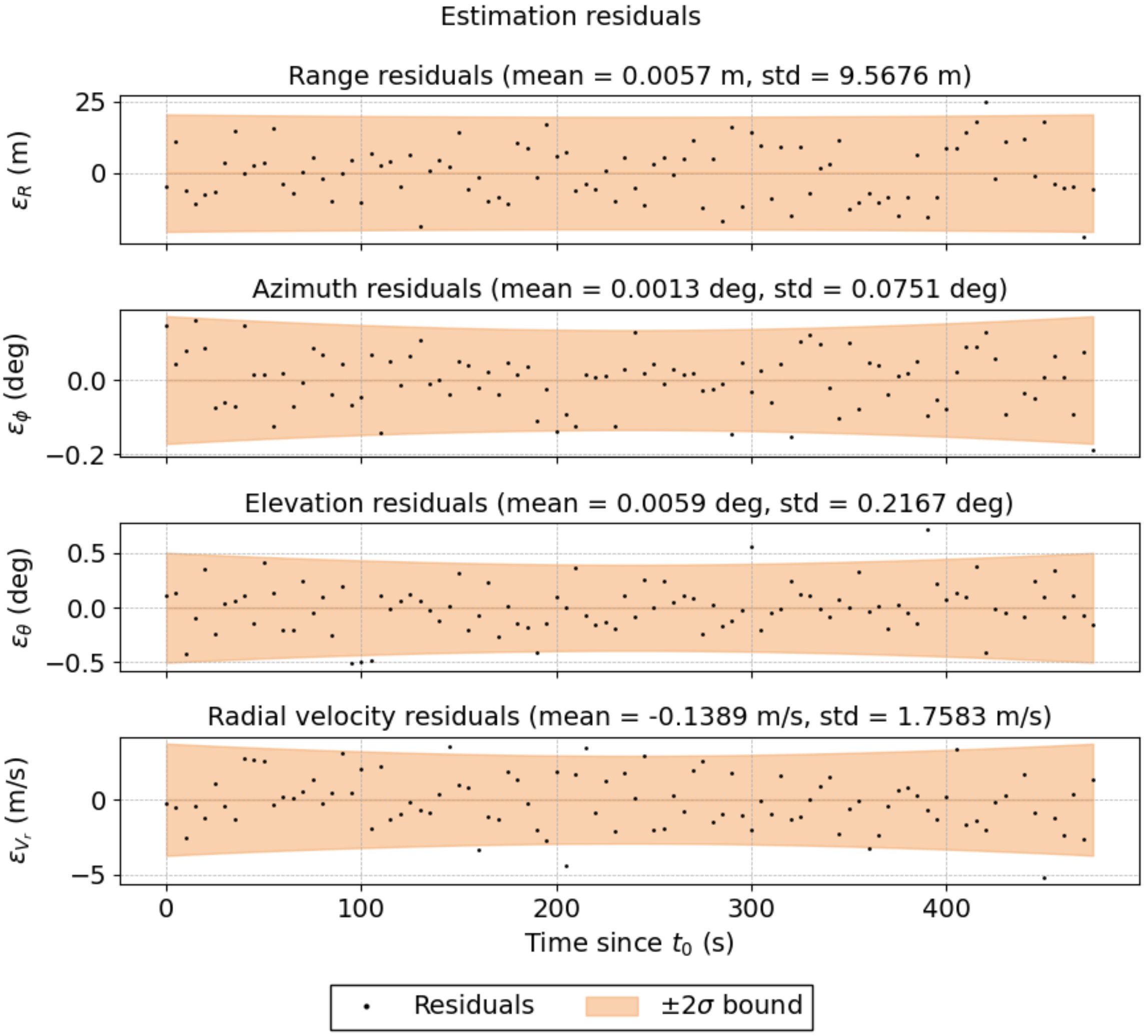

Figure 4.3: Post-fit estimation residuals for the unscented batch estimator (UBE), for the four different radar measurements. The dots represent the residuals and the red area represents the $\pm 2\sigma$-bounds of the measurements.

When generating measurements, Gaussian noise is added to the true measurements.

$$\vec{Y}_i = \vec{Y}_{\text{true},i} + \vec{n}_i, \tag{4.4}$$

where $\vec{Y}_i$ represents the noisy measurement, $\vec{Y}_{\text{true},i}$ is the true value, and $\vec{n}_i$ is the Gaussian noise with zero mean and variance σ^2. The estimator estimates the state $\hat{\vec{\mathbb{X}}}$, which is then converted to the measurement space to calculate the residuals. The process can be represented as follows:

- **State Estimation**: The estimator computes the estimated state $\hat{\vec{\mathbb{X}}}$.
- **Measurement Prediction**: The estimated state is transformed into the measurement space, resulting in predicted measurements $\hat{\vec{Y}}$.
- **Residual Calculation**: The residuals $\vec{r}$ are calculated as the difference between the actual noisy measurements $\vec{Y}$ and the predicted measurements $\hat{\vec{Y}}$:

$$\vec{r}_i = \vec{Y}_i - \hat{\vec{Y}}_i. \tag{4.5}$$

If the estimator is accurate, the residuals $\vec{r}_i$ should reflect the added noise $\vec{n}_i$ and thus appear as random noise within the specified bounds. From the figure is can be seen that for all the radar coordinates, the residuals have a mean close to zero, and a standard deviation close to the added noise. For reference, the standard deviation for range is around 10 m, for azimuth around 0.078 deg, for elevation around 0.22 deg and for radial velocity roughly 1.5 m/s (see Figure 3.9).

The estimator also produces the covariance of the estimate over time, which is a measure of confidence in the estimate. The $\pm 3\sigma$ bounds in Figure 4.4 represent the area where there is a 99.7% chance that the spacecraft is within. It is thus expected that the estimated state is within this $\pm 3\sigma$ bound. In Figure 4.4, the position error in Cartesian coordinates is shown. From the figure, it can be observed that the error is within the $\pm 3\sigma$ bounds, demonstrating good performance.

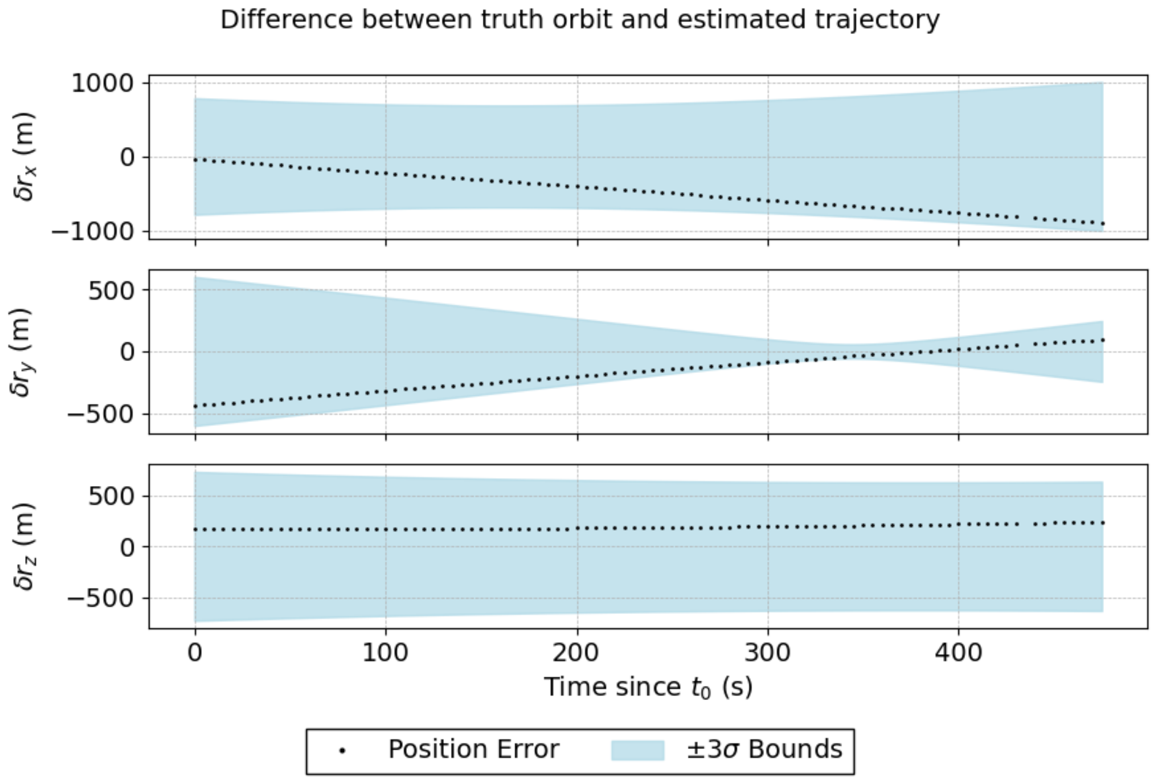

Figure 4.4: Difference in position between the estimated trajectory and the true state. The dots represent the error and the blue region represents the $\pm 3\sigma$-bounds of the covariance.

5

Conclusion and recommendations

In this chapter, the conclusions and recommendations of this study will be presented.

5.1. Conclusion

Space debris poses a significant challenge to current and future space missions. Before the space environment can be cleaned, the debris has to be located. There are numerous sensors that can track space objects such as the *Global Navigation Satellite System* (GNSS) and *Satellite Laser Ranging* (SLR). These methods can produce very accurate orbit estimations, however cooperation from the spacecraft is required. If a satellite is either tumbling, or has no power, these two methods will not work.

Telescopes and radars can measure objects without cooperation. Telescopes have the advantage that they can very accurately measure the spatial angles, which are lined up with the background stars. But during the day, or with cloudy weather conditions, the telescope is of no use. Radar does not have this problem, it can measure range, spatial angles and the radial velocity with respect to the sensor. Together with Thales Nederland, this study setup to find the most appropriate tracking algorithm for long range surveillance radars, and how to best use it.

The study aims to answer three questions. The first question is,

Which IOD algorithm shows the lowest RMSE with radar data?

For this question, four different IOD algorithms were tested, namely the *batch least squares estimator* (BLSE), *extended Kalman filter* (EKF), *unscented Kalman filter* (UKF) and the *unscented batch estimator* (UBE). These algorithms were applied to the trajectory data of the Sentinel-1A satellite, with initial states estimated via a Lambert targeting algorithm.

The study revealed that the UBE outperformed the other algorithms, providing the most accurate orbit estimation with and RMSE of 606.34 meters, and the fastest convergence with only 5 iterations. The other batch estimator (BLSE) has an RMSE of 717.78 meters and converged after 5 iterations, showing a slightly worse performance. For the sequential estimators, the UKF outperformed the BLSE with an RMSE of 670.61 meters, whilst the EKF has an RMSE of 1727.72 meters.

A key difference between batch estimators and sequential estimators lies in their respective performance characteristics. Sequential estimators tend to exhibit more variability in their error curves, whereas batch estimators produce smoother curves. This discrepancy arises from the fundamental nature of each approach. Sequential estimators continuously update their state estimates as new measurements are received, leading to ongoing fluctuations in their results. In contrast, batch estimators process the entire set of measurements simultaneously, seeking a global optimum that encompasses all data points. Consequently, batch estimators generate an initial state estimate that is subsequently propagated forward in time, resulting in a smooth and continuous trajectory.

It is worth noting that it is possible to achieve a smooth trajectory from sequential estimators by employing a technique known as smoothing. This involves using the estimated state at the end of processing all the measurements and then processing the measurements again, moving backward in time from the final step to the beginning. This method, was not considered within the scope of this project but could be investigated in future work. However, it is not expected to perform better than batch methods; rather, it allows sequential estimators to match the performance of batch estimators.

Furthermore, the study indicates that unscented estimators generally achieve slightly better performance compared to those that rely on traditional linearisation techniques. Orbit determination is inherently a highly non-linear problem, and conventional linearisation methods, which provide only a first-order approximation, may not fully capture the complex dynamics involved. Although the differences in performance are not vast, the unscented estimators show a better performance in handling non-linearities more effectively, leading to marginally more accurate orbit estimations.

A sensitivity analysis, comprising 100 Monte-Carlo runs with perturbed initial guesses, was conducted to evaluate the robustness of the algorithms. In this analysis, the UBE again demonstrated the lowest average RMSE and required the fewest average iterations for convergence. Interestingly, the BLSE outperformed the UKF in this scenario, suggesting that sequential estimators are more sensitive to initial conditions, as evidenced by the marked fluctuations in RMSE across the Monte-Carlo runs. Conversely, batch estimators exhibited minimal variability in RMSE and consistently converged to the same solution.

In conclusion, the UBE estimator is the most suitable method for tracking space objects with radar. It achieved better performance than the other three estimators in terms of RMSE and required fewer iterations for convergence. Additionally, it demonstrated notable robustness, making it a reliable choice for accurate orbit determination.

5.2. Recommendations

Whilst conducting this study, several intriguing questions emerged that were beyond its scope. Here are some recommendations for future research that can extend and build upon the findings of this study.

This study was confined to analysing a single orbit, specifically that of the Sentinel-1A satellite. Future research should examine how the proposed observation scenarios perform across various orbit types, which could provide a broader understanding of their applicability and effectiveness.

Another area for further exploration is identifying the essential forces to consider in the IOD algorithm. In this study, a comprehensive force model was used, which is computationally demanding. It may be worthwhile to investigate whether considering only the J_2 effect is sufficient to achieve approximate estimates for reacquisition. Furthermore, it would be insightful to determine what additional benefits, if any, are gained by incorporating more complex accelerations into the dynamics model.

By addressing these recommendations, future research can deepen our understanding of orbit determination with radar and enhance the methods and models used in this field.

References

[1] A. Gorman. “Space Debris, Space Situational Awareness and Cultural Heritage Management in Earth Orbit”. In: *Commercial and Military Uses of Outer Space* (2021), pp. 133–151.

[2] N. AlDahoul, H. Karim, A. Castro, and M. Tan. *Localization and classification of space objects using EffientDet detector for space situational awareness*. en. 2022. URL: www.nature.com/scientificreports.

[3] H. Klinkrad. “Hazard of Orbital Debris”. In: *Handbook of Cosmic Hazards and Planetary Defense* (2015), pp. 808–834.

[4] ”ESA”. *Space Environment Statistics,” Space Environment Statistics, Space Debris User Portal*. 2023. URL: https://sdup.esoc.esa.int/discosweb/statistics/..

[5] A. Lawrence, M. L. Rawls, M. Jah, A. Boley, F. Di Vruno, S. Garrington, M. Kramer, S. Lawler, J. McDowell, and M. McCaughrean. “The case for space environmentalism”. In: *Nature Astronomy* (2022).

[6] ”NASA”. “Satellite Collision Leaves Significant Debris Clouds”. In: *Orbital Debris, Quarterly News* 13 (2009).

[7] ”ESA. *About space debris*. URL: https://www.esa.int/Space_Safety/Space_Debris/About_space_debris.

[8] D. Kessler and B. Cour-Palais. “Collision Frequency of Artificial Satellites: The Creation of a Debris Belt”. In: *Journal of Geophysical Research* 83 (1978), pp. 2637–2646.

[9] J. Kepler. *Astronomia Nova*. Princeton University Press, 1609.

[10] J. Kepler. *Tabulae Rudolpinae*. Gorlitz, 1627.

[11] J. Lambert. *Insigniores Orbitae Cometarum Proprietates*. Eberhard Klett, 1761.

[12] J. Lagrange. *Mécanique Analytique*. Ve Courcier, 1811.

[13] C. Gauss. *Theoria Motus Corporum Coelestium in Sectionibus Conicis Solem Ambientium*. Perthes und Besser, 1809.

[14] D. Vallado. *Fundamentals of Astrodynamics and Applications*. 2nd. Netherlands: Kluwer Academic Publisher, 2001.

[15] P. Escobal. *Methods of Orbit Determination*. New York: John Wiley and Sons, 1965.

[16] R. Gooding. “A New Procedure for the Solution of the Classical Problem of Minimal Orbit Determination from Three Lines of Sight”. In: *Celestical Mechanics and Dynamical Astronomy* 66.4 (1996), pp. 387–423.

[17] D. Hobbs and P. Bohm. “Precise Orbit Determination for Low Earth Orbit Satellites”. In: *Annals of the Marie Curie Fellowship Association* (2006).

[18] R. Merwe and E. Wan. *The Square-Root Unscented Kalman Filter for State Estimation and Parameter Estimation*. Oregon Graduate Institute of Science and Technology, 2005.

[19] M. Noorgard and O. Ravn. “New Developments in State Estimation for Nonlinear Systems”. In: *Automatica* 36 (2000), pp. 1627–1638.

[20] G. Evensen. “The Ensemble Kalman Filter: Theoretical formulation and practical implementation”. In: *Ocean Dynamics* 53 (2003), pp. 343–367.

[21] R. Novoselov, S. Herman, S. Gadaleta, and A. Poore. “Mitigating the Effects of Residual Biases with Schmidt-Kalman Filtering”. In: *7th International Conference on Information Fusion (FUSION* (2005), pp. 358–365.

[22] S. Bonnabel, P. Martin, and E. Salaun. “Invariant Extended Kalman Filter: theroy and application to a velocity-aided attitude estimation problem”. In: *Proceedings of the 48th IEEE Conference on Decision and Control* (2009).

[23] A. Haug. “A Tutorial on Bayesian Estimation and Tracking Techniques Applicable to Nonlinear and Non-Gaussian Processes”. In: *MITRE Technical Report,* (2005).

[24] R. Kalman. “A New Approach to Linear Filtering and Prediction Problems”. In: *Transactions of the ASME–Journal of Basic Engineering* 82 (1960), pp. 35–45.

[25] R. Kalman and R. Bucy. “New Results in Linear Filtering and Prediction Theory”. In: *Journal of Basic Engineering* 83.1 (1961), pp. 95–108.

[26] A. Gelb. *Appied Optimal Estimation*. The MIT Press, 1974.

[27] S. Servadio and R. Zanetti. “Differential Algebra-Based Multiple Gaussian Particle Filter for Orbit Determination”. In: *Journal of Optimzation Theory and Applications* 191 (2021), pp. 459–485.

[28] J. Junkins and P. Singla. “How nonlinear is it? A tuorial on nonlinearity of orbit and attitude dynamics”. In: *The Journal of the Astronautical Sciences* 52.1 (2004), pp. 7–60.

[29] S. Julier and J. Uhlmann. “Unscented filtering and nonlinear estimation”. In: *Proceedings of the IEEE* 92.3 (2004), pp. 401–422.

[30] S. Julier, J. Uhlmann, and H. Durrant-Whyte. “A new approach for filtering nonlinear systems”. In: *Proceedings of 1995 American Control Conference*. Vol. 3. 1995, pp. 1628–1632.

[31] J. Crassidis and F. Markley. “Unscented filtering for spacecraft attitude estimation”. In: *Journal for Guidance, Control and Dynamics* 26.4 (2003), pp. 536–542.

[32] D. Lee and K. Alfriend. “Adaptive sigma point fitering for state and parameter estimation”. In: *AIAA/AAS Astrodynamics Conference* (2004).

[33] D. Lee and K. Alfriend. “Sigma point filtering for sequential orbit estimation and prediction”. In: *Journal for Spacecraft and Rockets* 44.2 (2007), pp. 388–398.

[34] A. Farina, B. Ristic, and D. Benvenuti. “Tracking a ballistic target: Comparison of several nonlinear filters”. en. In: *IEEE Transaction on Aerospace and Electronics* 38.3 (2002), pp. 864–867.

[35] G. Bierman. *Factorizing Methods for Discrete Sequential estimation*. New York: Academic Press, 1977.

[36] A. Brysen and Y. Ho. *Aplpied Optimal control*. Washington DC: Hemisphere, 1975.

[37] B. Taply, B. Schutz, and G. Born. *Statistical Orbit Determination*. Elsevier, 2004.

[38] E.-S. Park, S.-Y. Park, K.-M. Roh, and K.-H. Choi. “Satellite orbit determination using a batch filter based on the unscented transformation”. In: *Aerospace Science and Technology* 14 (2010), pp. 387–396.

[39] D. Bai. “Orbit Determination Based on Particle Filtering Algorithm”. In: *Lecture Notes in Electrical Engineering* 439, vol. 3 (2017), pp. 3–10.

[40] J. Carpenter, P. Cliffordy, and P. Fearnhead. “An Improved Particle Filter for nonlinear problems”. In: *IEE Proceedings - Radar, Sonar and Navigation* 146.1 (1999), pp. 2–7.

[41] J. Kotecha and P. Djuric. “Gaussian Particle Filtering”. In: *IEEE Transactions on Signal Processing* 51.10 (2003), pp. 2592–2601.

[42] M. Arulampalam, S. Maskell, N. Gordon, and T. Clapp. “A tutorial on particle filters for online nonlinear/non-Gaussian Bayesian tracking”. In: *IEEE Transactions on Signal Processing* 50.2 (2002), pp. 174–188.

[43] A. Milani, G. Gronchi, M. Michieli Vitturi, and Z. Knezevic. “Orbit Determination with Very Short Arcs: I”. In: *Admissible Regions,” Celestial Mechanics and Dynamical Astronomy* 90 (2004), pp. 59–87.

[44] G. Tommei, A. Milani, and A. Rossi. “Orbit determination of space debris: admissible region”. In: *Celestial Mechanics and Dynamical Astronomy* 97 (2007), pp. 289–304.

[45] C. Roscoe, I. Hussein, and M. Wilkins. *The Probablistic Admissible Region with Additionl Constraints*. 2014.

[46] H. Cai, I. Hussein, and M. jah. “Possibilistic admissble region using outer probability measure theory”. In: *Acta Astronautica* 177 (2020), pp. 246–257.

[47] H. Cai, Y. Yang, S. Gehly, S. Wu, and K. Zhang. “Improved tracklet association for space objects using short-arc optical measurements”. In: *Acta Astronatuica* 151 (2018), pp. 836–847.

[48] J. Maruskin, D. Scheeres, and K. Alfriend. “Correlation of optical observations of objects in Earth orbit”. In: *Journal of Guidance, Control, and Dynamics* 32.1 (2009), pp. 194–209.

[49] K. Fujimoto and D. Scheers. “Correlation of optical observations of Earth-orbiting objects and initial orbit determination”. In: *Journal of Guidance, Control, and Dynamics* 35.1 (2012), pp. 208–221.

[50] J. Siminiski, O. Montenbruck, H. Fiedles, and T. Schildknecht. “Short-arc tracklet association for geostationary objects”. In: *Advanced Space Research* 53.8 (2014), pp. 1184–1194.

[51] K. DeMars and M. Jah. “Probabilistic initial orbit determination using Guassian Mixture Models”. In: *Journal of Guidance, Control, and Dynamics* 36.5 (2013), pp. 1324–1335.

[52] ”THALES”. *SMART-L Multi Mission*. URL: `https://www.thalesgroup.com/en/markets/defence-and-security/naval-forces/above-water-warfare/smart-l-multi-mission/`.

[53] F. Guo, Y. Yang, F. Ma, Y. Zhu, H. Liu, and X. Zhang. “Instantaneous velocity determination and positioning using Doppler shift from a LEO constellation”. In: *Satellite Navigation* (2023).

[54] K. Jiang, W. Li, J. Geng, Q. Zhao, and L. Jingnan. “Precise orbit determination of Haiyang-2D using onboard BDS-3 B1C/B2a observations with ambiguity resolution”. In: *Satellite Navigation* (2023).

[55] H. Zhang, B. Ju, D. Gu, Y. Lui, K. Shao, X. Duan, and Z. Huang. “Precise orbit determination for TH02-02 satellites based on BDS3 and GPS observations”. In: *Chinese Journal for Aeronautics* (2023), pp. 457–485.

[56] G. Escribano, M. Sanjurjo-Rivo, J. Siminiski, and D. Escobar. “A filter for tracking non-cooperative low-thrust satellites using surveillance radar data”. In: *Acta Astronautica* (2023), pp. 694–707.

[57] B. Hua, G. Yang, Y. Wu, and Z. Chen. "A multi-satellite co-tracking method for a single space target based on adaptive distrubuted spherical simplex information-weighted consensus filter". In: *Advances in Space Research* (2023), pp. 2640–2655.

[58] M. Richards, J. Scheer, and W. Holm. *Principles of Modern Radar Vol.1: Basic Principles*. 2010.

[59] M. Skolnik. *Introduction to Radar Systems*. 3rd ed. McGraw-Hill, 2002.

[60] D. Barton. *Radar Equations for Modern Radar*. Artech House, 2013.

[61] P. N. C. Nooy. *Doelsignaturen & Meetinstrumenten*. Tech. rep. Internal Thales publication. Hengelo: Thales, 1995.

[62] P. Swerling. *Probability of Detection for Fluctuating Targets*. ASTIA Document AD 80638. Armed Services Technical Information Agency, Mar. 1954.

[63] R. Manasse. "Range and Velocity Accuracy from Radar Measurements". Internal memo. Not generally available. Lexington, MA, Feb. 1955.

[64] D. G. Altman and J. M. Bland. "Standard deviations and standard errors". In: *BMJ* 331.7521 (2005), p. 903. ISSN: 0959-8138. DOI: 10.1136/bmj.331.7521.903. eprint: https://www.bmj.com/content/331/7521/903.full.pdf. URL: https://www.bmj.com/content/331/7521/903.

[65] M. Skolnik. *Radar Handbook*. 3rd ed. McGraw-Hill, 2008.

[66] D. Barton. *Radar System Analysis and Modeling*. Artech House radar library. Artech House, 2005. ISBN: 9781580536813. URL: https://books.google.nl/books?id=GaVTAAAAMAAJ.

[67] R. Ostrovit͡ianov and F. Basalov. *Statistical Theory of Extended Radar Targets: A Translation from the Russian of Statisticheskaya Teoriya Radiolokatsii Protyazhennyz [sic] Tselei*. Artech House, 1985. ISBN: 9780890061442. URL: https://books.google.nl/books?id=97o2AQAAIAAJ.

[68] NASA. *International Space Station*. 2023. URL: https://www.nasa.gov/reference/international-space-station/ (visited on 03/25/2024).

[69] Electronic Trajectory Measurements Group. *Error Sources Applicable to Precision Trajectory Radar Calibration*. Tech. rep. 255-80. White Sands Missile Range, New Mexico 88002: Range Commanders Council, White Sands Missile Range, 1980. URL: https://apps.dtic.mil/sti/tr/pdf/ADA091654.pdf (visited on 04/09/2024).

[70] K. F. Wakker. *Fundamentals of Astrodynamics*. Delft, The Netherlands: Institutional Repository Library, Delft University of Technology, Jan. 2015. ISBN: 978-94-6186-419-2. URL: http://repository.tudelft.nl.

[71] 'Navigation and A. I. Facility'. "An overview of reference frames and coordinate systems in the SPICE context". In: (2023).

[72] *ITRF2020*. 2020. URL: https://itrf.ign.fr/en/solutions/itrf2020.

[73] G. Petit and B. Luzum. *IERS Conventions (2010)*. IERS Technical Note 36. Frankfurt am Main: Verlag des Bundesamts für Kartographie und Geodäsie, 2010, p. 179.

[74] National Center for Geospatial Intelligence Standards (NCGIS), National Geospatial-Intelligence Agency (NGA). *NGA.STND.0036_1.0.0_WGS84: The World Geodetic System 1984*. Technical Standard. National Geospatial-Intelligence Agency, 2014. URL: https://gwg.nga.mil/gwg/focus-groups/World_Geodetic_System_&_Geomatics_(WGSG)_Focus_Gro.html.

[75] I. Newton. *Philosophiae Naturalis Principia Mathematica*. 1687.

[76] A. Roy. *Orbital Motion*. CRC Press, 1978. ISBN: 9780852743225. URL: https://books.google.nl/books?id=0agNAQAAIAAJ.

[77] M. H. Kaplan. *Modern Spacecraft Dynamics and Control*. New York: John Wiley & Sons, 1976.

[78] P. Fitzpatrick. *Principles of Celestial Mechanics*. Academic Press, 1970. ISBN: 9780122579509. URL: https://books.google.nl/books?id=GJd-AAAAIAAJ.

[79] K. Lambeck. *Geophysical Geodesy: The Slow Deformations of the Earth*. Oxford: Clarendon Press, 1988.

[80] E. Igwenagu. *Fundamentals of research methodology and data collection*. Lambert Academic Publishing, 2016.

[81] Google Maps. *Location of SMART-L MM/N radar tower*. 2024. URL: https://www.google.com/maps/place/SMART-L+MM%2FN+radartoren/@52.2470124,6.7691421,19.77z/data=!4m6!3m5!1s0x47b80d3aa2e05f11:0xac280f7219d8a90d!8m2!3d52.247051!4d6.7693464!16s%2Fg%2F11swd590gd?entry=ttu (visited on 03/19/2024).

[82] Thales Nederland. *Vandaag is de eerste nieuwe SMART-L MM geplaatst op Zr.Ms. De Zeven Provinciën*. 2023. URL: https://www.facebook.com/ThalesNederland/posts/vandaag-is-de-eerste-nieuwe-smart-l-mm-geplaatst-op-zrms-de-zeven-provinci%C3%ABn-de-/2577404772288401/?locale=nl_NL&checkpoint_src=any (visited on 03/19/2024).

[83] H. Wilden, C. Kirchner, O. Peters, N. Ben Bekhti, A. Brenner, and T. Eversberg. "GESTRA — A phased-array based surveillance and tracking radar for space situational awareness". In: *2016 IEEE International Symposium on Phased Array Systems and Technology (PAST)*. 2016, pp. 1–5. DOI: 10.1109/ARRAY.2016.7832621.

[84] E.-J. Choi, S. Cho, J. Jo, J.-H. Park, T. Chung, J.-H. Park, H. Jeon, A. Yun, and Y. Lee. "Performance Analysis of Sensor Systems for Space Situational Awareness". In: *Journal of Astronomy and Space Science* 34 (Dec. 2017), pp. 303–313. DOI: 10.5140/JASS.2017.34.4.303.

[85] J. Lee, E. J. Choi, H.-W. Moon, J. Park, S. Cho, J. H. Park, and J. H. Jo. "Design of L-Band-Phased Array Radar System for Space Situational Awareness". In: *The Journal of Korean Institute of Electromagnetic Engineering and Science* 29.3 (Mar. 2018), pp. 214–224. ISSN: 1226-3133. DOI: 10.5515/KJKIEES.2018.29.3.214. URL: http://dx.doi.org/10.5515/KJKIEES.2018.29.3.214.

[86] "ESA". *POD Products and Requirements*. URL: https://sentinels.copernicus.eu/web/sentinel/technical-guides/sentinel-1-sar/pod/products-requirements.

[87] European Space Agency. *Sentinel-1*. URL: https://www.esa.int/Enabling_Support/Operations/Sentinel-1_operations (visited on 03/11/2024).

[88] W. Wagner. *Sentinel-1: Chancen und Herausforderungen für die Wissenschaft*. 2015. URL: https://www.d-copernicus.de/fileadmin/Content/pdf/Forum_2015/Wagner_TU-Wien.pdf (visited on 03/22/2024).

[89] E. Attema, P. Bargellini, P. Edwards, G. Levrini, S. Lokas, L. Moeller, B. Rosich-Tell, P. Secchi, R. Torres, M. Davidson, and P. Snoeij. *Sentinel-1: The Radar Mission for GMES Operational Land and Sea Services*. Aug. 2007. URL: https://www.esa.int/esapub/bulletin/bulletin131/bul131a_attema.pdf (visited on 03/11/2024).

[90] Heavens-Above. *Sentinel 1A - Orbit*. Heavens-Above. 2024. URL: https://www.heavens-above.com/orbit.aspx?satid=39634 (visited on 01/05/2024).

[91] European Space Agency. *Sentinel-1A Satellite Mass History File*. Copernicus Sentinel Data. 2024. URL: https://sentinels.copernicus.eu/web/sentinel/technical-guides/sentinel-1-sar/pod/satellite-parameters (visited on 03/12/2024).

[92] *Orekit - An open-source library for space flight dynamics*. URL: https://www.orekit.org/.

[93] J. Steward. *Calculus, Early Transcendentals*. 8th ed. Brooks/Cole, 2015.

A

Derivation batch least squares estimator

$$\vec{y} = \boldsymbol{H}\vec{x} + \vec{\epsilon} \tag{A.1}$$

To minimise the observation residual, an estimate of $\vec{x}$ has to be made such that a cost function is minimised,

$$\boldsymbol{J}\left(\vec{x}\right) = \frac{1}{2}\vec{\epsilon}^{T}\vec{\epsilon} \tag{A.2}$$

Rewriting Equation A.1 into,$\vec{\epsilon} = \vec{y} - \boldsymbol{H}\vec{x}$ and substituting into Equation A.2 yields,

$$\boldsymbol{J}(t) = \frac{1}{2}\left(\vec{y} - \boldsymbol{H}\vec{x}\right)^{T}\left(\vec{y} - \boldsymbol{H}\vec{x}\right) \tag{A.3}$$

Taply et al. [37], provide proof that this expression has a unique minima when,

$$\frac{\partial \boldsymbol{J}}{\partial \vec{x}} = 0 \text{ and, } \delta\vec{x}^{T}\frac{\partial^2 \boldsymbol{J}}{\partial \vec{x}^2}\delta\vec{x} > 0 \tag{A.4}$$

With the first condition, the least squares estimate of $\vec{x}$, denoted as $\hat{x}$, can be calculated,

$$\frac{\partial \boldsymbol{J}}{\partial \vec{x}} = 0 = -\left(\vec{y} - \boldsymbol{H}\vec{x}\right)^{T}\boldsymbol{H} = -\boldsymbol{H}^{T}\left(\vec{y} - \boldsymbol{H}\vec{x}\right) \tag{A.5}$$

The value of $\vec{x}$, that satisfies Equation A.5 is $\hat{x}$. Hence,

$$\left(\boldsymbol{H}^{T}\boldsymbol{H}\right)\hat{x} = \boldsymbol{H}^{T}\vec{y} \tag{A.6}$$

Solving for $\hat{x}$, yields the final solution for the least squares estimate,

$$\hat{x} = \left(\boldsymbol{H}^{T}\boldsymbol{H}\right)^{-1}\boldsymbol{H}^{T}\vec{y} \tag{A.7}$$

As a performance parameter, the best estimate of the observation error $\hat{\epsilon}$ can be calculated,

$$\hat{\epsilon} = \vec{y} - \boldsymbol{H}\hat{x} \tag{A.8}$$

A very important aspect that the batch least squares estimator does not account for, is the quality of the observations. It is likely that not every observation has the same accuracy, hence they should not be weighted all equally.

B

Derivation of the observation matrix $\tilde{\boldsymbol{H}}_k$

The observation vector $\vec{Y}_k$ at time k is defined as,

$$\vec{Y}_k\left(\vec{\mathbb{X}}\right) = \begin{bmatrix} R \\ \phi \\ \theta \\ V_r \end{bmatrix} = \begin{bmatrix} |\vec{r}| \\ \text{arctan}\left(\frac{x}{y}\right) \\ \text{arcsin}\left(\frac{z}{|\vec{r}|}\right) \\ \frac{\vec{r}\cdot\vec{r}}{|\vec{r}|} \end{bmatrix} = \begin{bmatrix} \sqrt{x^2+y^2+z^2} \\ \text{arctan}\left(\frac{x}{y}\right) \\ \text{arcsin}\left(\frac{z}{\sqrt{x^2+y^2+z^2}}\right) \\ \frac{x\dot{x}+y\dot{y}+z\dot{z}}{\sqrt{x^2+y^2+z^2}} \end{bmatrix} \tag{B.1}$$

where $\vec{\mathbb{X}} = \begin{bmatrix} x & y & z & \dot{x} & \dot{y} & \dot{z} \end{bmatrix}$ is the Cartesian spacecraft state. With these relations, the partial derivatives of the observations can be derived with respect to the Cartesian state, resulting in the Jacobian:

$$\tilde{\boldsymbol{H}}_k = \begin{bmatrix} \frac{\partial R}{\partial x} & \frac{\partial R}{\partial y} & \frac{\partial R}{\partial z} & \frac{\partial R}{\partial \dot{x}} & \frac{\partial R}{\partial \dot{y}} & \frac{\partial R}{\partial \dot{z}} \\ \frac{\partial \phi}{\partial x} & \frac{\partial \phi}{\partial y} & \frac{\partial \phi}{\partial z} & \frac{\partial \phi}{\partial \dot{x}} & \frac{\partial \phi}{\partial \dot{y}} & \frac{\partial \phi}{\partial \dot{z}} \\ \frac{\partial \theta}{\partial x} & \frac{\partial \theta}{\partial y} & \frac{\partial \theta}{\partial z} & \frac{\partial \theta}{\partial \dot{x}} & \frac{\partial \theta}{\partial \dot{y}} & \frac{\partial \theta}{\partial \dot{z}} \\ \frac{\partial V_r}{\partial x} & \frac{\partial V_r}{\partial y} & \frac{\partial V_r}{\partial z} & \frac{\partial V_r}{\partial \dot{x}} & \frac{\partial V_r}{\partial \dot{y}} & \frac{\partial V_r}{\partial \dot{z}} \end{bmatrix} = \begin{bmatrix} J_R\left(\vec{\mathbb{X}}\right) \\ J_\phi\left(\vec{\mathbb{X}}\right) \\ J_\theta\left(\vec{\mathbb{X}}\right) \\ J_{V_r}\left(\vec{\mathbb{X}}\right) \end{bmatrix} \tag{B.2}$$

B.1. Range, R

For range, the partial derivatives for position can be derived using the chain rule [93].
For x-position:

$$\frac{\partial R}{\partial x} = \frac{1}{2\sqrt{x^2+y^2+z^2}}\frac{\partial}{\partial x}\left(x^2+y^2+z^2\right)$$

$$\frac{\partial R}{\partial x} = \frac{x}{\sqrt{x^2+y^2+z^2}} = \frac{x}{R} \tag{B.3}$$

For y-position:

$$\frac{\partial R}{\partial y} = \frac{1}{2\sqrt{x^2+y^2+z^2}} \frac{\partial}{\partial y}\left(x^2+y^2+z^2\right)$$

$$\frac{\partial R}{\partial y} = \frac{y}{\sqrt{x^2+y^2+z^2}} = \frac{y}{R} \tag{B.4}$$

For z-position:

$$\frac{\partial R}{\partial z} = \frac{1}{2\sqrt{x^2+y^2+z^2}} \frac{\partial}{\partial z}\left(x^2+y^2+z^2\right)$$

$$\frac{\partial R}{\partial z} = \frac{z}{\sqrt{x^2+y^2+z^2}} = \frac{x}{R} \tag{B.5}$$

For x-velocity:

$$\frac{\partial R}{\partial \dot{x}} = 0 \tag{B.6}$$

For y-velocity:

$$\frac{\partial R}{\partial \dot{y}} = 0 \tag{B.7}$$

For z-velocity:

$$\frac{\partial R}{\partial \dot{z}} = 0 \tag{B.8}$$

Summarised, the Jacobian of range with respect to the Cartesian satellite state is,

$$J_R\left(\vec{\mathbb{X}}\right) = \begin{bmatrix} \frac{x}{R} & \frac{y}{R} & \frac{z}{R} & 0 & 0 & 0 \end{bmatrix} \tag{B.9}$$

B.2. Azimuth, ϕ

For azimuth, the partial derivatives can derived using the chain rule [93].
For the x-position:

$$\frac{\partial \phi}{\partial x} = \frac{1}{1+\left(\frac{x}{y}\right)^2} \frac{\partial}{\partial x} \frac{x}{y}$$

$$\frac{\partial \phi}{\partial x} = \frac{1}{1+\left(\frac{x}{y}\right)^2} \frac{1}{y} = \frac{y}{x^2+y^2} \tag{B.10}$$

For the y-position:

$$\frac{\partial \phi}{\partial y} = \frac{1}{1+\left(\frac{x}{y}\right)^2} \frac{\partial}{\partial y} \frac{x}{y}$$

$$\frac{\partial \phi}{\partial y} = \frac{1}{1+\left(\frac{x}{y}\right)^2}\frac{-x}{y^2} = -\frac{x}{x^2+y^2} \tag{B.11}$$

For the z-position:

$$\frac{\partial \phi}{\partial z} = 0 \tag{B.12}$$

For the x-velocity:

$$\frac{\partial \phi}{\partial \dot{x}} = 0 \tag{B.13}$$

For the y-velocity:

$$\frac{\partial \phi}{\partial \dot{y}} = 0 \tag{B.14}$$

For the z-velocity:

$$\frac{\partial \phi}{\partial \dot{z}} = 0 \tag{B.15}$$

Summarised, the Jacobian of azimuth with respect to the Cartesian spacecraft state is,

$$J_\phi\left(\vec{\mathbb{X}}\right) = \begin{bmatrix} \frac{y}{x^2+y^2} & -\frac{x}{x^2+y^2} & 0 & 0 & 0 & 0 \end{bmatrix} \tag{B.16}$$

B.3. Elevation, θ

For elevation, the partial derivatives can be derived using the chain rule [93].
For x-position:

$$\frac{\partial \theta}{\partial x} = \frac{1}{\sqrt{1-\left(\frac{z}{\sqrt{x^2+y^2+z^2}}\right)^2}}\frac{\partial}{\partial x}\frac{z}{\sqrt{x^2+y^2+z^2}}$$

$$\frac{\partial \theta}{\partial x} = \frac{1}{\sqrt{1-\left(\frac{z}{\sqrt{x^2+y^2+z^2}}\right)^2}}\frac{-zx}{\sqrt{x^2+y^2+z^2}^3} = -\frac{zx}{R^2\sqrt{x^2+y^2}} \tag{B.17}$$

For y-position:

$$\frac{\partial \theta}{\partial y} = \frac{1}{\sqrt{1-\left(\frac{z}{\sqrt{x^2+y^2+z^2}}\right)^2}}\frac{\partial}{\partial y}\frac{z}{\sqrt{x^2+y^2+z^2}}$$

$$\frac{\partial \theta}{\partial y} = \frac{1}{\sqrt{1-\left(\frac{z}{\sqrt{x^2+y^2+z^2}}\right)^2}}\frac{-zy}{\sqrt{x^2+y^2+z^2}^3} = -\frac{zy}{R^2\sqrt{x^2+y^2}} \tag{B.18}$$

For z-position:

$$\frac{\partial\theta}{\partial z} = \frac{1}{\sqrt{1-\left(\frac{z}{\sqrt{x^2+y^2+z^2}}\right)^2}}\frac{\partial}{\partial z}\frac{z}{\sqrt{x^2+y^2+z^2}}$$

$$\frac{\partial\theta}{\partial z} = \frac{1}{\sqrt{1-\left(\frac{z}{\sqrt{x^2+y^2+z^2}}\right)^2}}\frac{\sqrt{x^2+y^2}}{\sqrt{x^2+y^2+z^2}^3} = \frac{z\sqrt{x^2+y^2}}{R^2} \tag{B.19}$$

For x-velocity:

$$\frac{\partial\theta}{\partial\dot{x}} = 0 \tag{B.20}$$

For y-velocity:

$$\frac{\partial\theta}{\partial\dot{y}} = 0 \tag{B.21}$$

For z-velocity:

$$\frac{\partial\theta}{\partial\dot{z}} = 0 \tag{B.22}$$

Summarised, the Jacobian of elevation with respect to the Cartesian spacecraft state is,

$$J_\theta\left(\vec{\mathbb{X}}\right) = \begin{bmatrix} -\frac{zx}{R^2\sqrt{x^2+y^2}} & -\frac{zy}{R^2\sqrt{x^2+y^2}} & \frac{z\sqrt{x^2+y^2}}{R^2} & 0 & 0 & 0 \end{bmatrix} \tag{B.23}$$

B.4. Radial velocity V_r (range rate)

For the range, the partial derivatives can be derived using the quotient rule [93]:

$$h(x) = \frac{f(x)}{h(x)} \rightarrow \frac{dh(x)}{dx} = \frac{\frac{df(x)}{dx}g(x) - f(x)\frac{g(x)}{dx}}{g(x)^2} \tag{B.24}$$

For the x-position, the aforementioned becomes:

$$\frac{\partial V_r}{\partial x} = \frac{\frac{\partial}{\partial x}\left(x\dot{x}+y\dot{y}+z\dot{z}\right)\sqrt{x^2+y^2+z^2} - \frac{\partial}{\partial x}\left(\sqrt{x^2+y^2+z^2}\right)\left(x\dot{x}+y\dot{y}+z\dot{z}\right)}{\left(\sqrt{x^2+y^2+z^2}\right)^2} \tag{B.25}$$

where,

$$\frac{\partial}{\partial x}\left(x\dot{x}+y\dot{y}+z\dot{z}\right) = \dot{x} \tag{B.26}$$

and,

$$\frac{\partial}{\partial x}\left(\sqrt{x^2+y^2+z^2}\right)=\frac{x}{\sqrt{x^2+y^2+z^2}} \tag{B.27}$$

Substituting Equation B.26 and Equation B.27 into Equation B.25, yields,

$$\frac{\partial V_r}{\partial x}=\frac{\dot{x}\sqrt{x^2+y^2+z^2}-\frac{x}{\sqrt{x^2+y^2+z^2}}\left(x\dot{x}+y\dot{y}+z\dot{z}\right)}{\left(\sqrt{x^2+y^2+z^2}\right)^2}=\frac{-xy\dot{y}-xz\dot{z}+\dot{x}\left(y^2+z^2\right)}{R^3} \tag{B.28}$$

For the y-position:

$$\frac{\partial V_r}{\partial y}=\frac{\frac{\partial}{\partial y}\left(x\dot{x}+y\dot{y}+z\dot{z}\right)\sqrt{x^2+y^2+z^2}-\frac{\partial}{\partial y}\left(\sqrt{x^2+y^2+z^2}\right)\left(x\dot{x}+y\dot{y}+z\dot{z}\right)}{\left(\sqrt{x^2+y^2+z^2}\right)^2} \tag{B.29}$$

where,

$$\frac{\partial}{\partial y}\left(x\dot{x}+y\dot{y}+z\dot{z}\right)=\dot{x} \tag{B.30}$$

and,

$$\frac{\partial}{\partial y}\left(\sqrt{x^2+y^2+z^2}\right)=\frac{x}{\sqrt{x^2+y^2+z^2}} \tag{B.31}$$

Substituting Equation B.30 and Equation B.31 into Equation B.29, yields,

$$\frac{\partial V_r}{\partial y}=\frac{\dot{x}\sqrt{x^2+y^2+z^2}-\frac{x}{\sqrt{x^2+y^2+z^2}}\left(x\dot{x}+y\dot{y}+z\dot{z}\right)}{\left(\sqrt{x^2+y^2+z^2}\right)^2}=\frac{-xy\dot{x}-yz\dot{z}+\dot{y}\left(x^2+z^2\right)}{R^3} \tag{B.32}$$

For the z-position:

$$\frac{\partial V_r}{\partial z}=\frac{\frac{\partial}{\partial z}\left(x\dot{x}+y\dot{y}+z\dot{z}\right)\sqrt{x^2+y^2+z^2}-\frac{\partial}{\partial z}\left(\sqrt{x^2+y^2+z^2}\right)\left(x\dot{x}+y\dot{y}+z\dot{z}\right)}{\left(\sqrt{x^2+y^2+z^2}\right)^2} \tag{B.33}$$

where,

$$\frac{\partial}{\partial z}\left(x\dot{x}+y\dot{y}+z\dot{z}\right)=\dot{x} \tag{B.34}$$

and,

$$\frac{\partial}{\partial z}\left(\sqrt{x^2+y^2+z^2}\right)=\frac{x}{\sqrt{x^2+y^2+z^2}} \tag{B.35}$$

Substituting Equation B.34 and Equation B.35 into Equation B.33, yields,

$$\frac{\partial V_r}{\partial z}=\frac{\dot{x}\sqrt{x^2+y^2+z^2}-\frac{x}{\sqrt{x^2+y^2+z^2}}\left(x\dot{x}+y\dot{y}+z\dot{z}\right)}{\left(\sqrt{x^2+y^2+z^2}\right)^2}=\frac{-zx\dot{x}-zy\dot{y}+\dot{z}\left(x^2+y^2\right)}{R^3} \tag{B.36}$$

For the x-velocity:

$$\frac{\partial V_r}{\partial \dot{x}} = \frac{1}{\sqrt{x^2+y^2+z^2}} \frac{\partial}{\partial \dot{x}} \left(x\dot{x} + y\dot{y} + z\dot{z}\right)$$

$$\frac{\partial V_r}{\dot{x}} = \frac{x}{\sqrt{x^2+y^2+z^2}} = \frac{x}{R} \tag{B.37}$$

For the y-velocity:

$$\frac{\partial V_r}{\partial \dot{y}} = \frac{1}{\sqrt{x^2+y^2+z^2}} \frac{\partial}{\partial \dot{y}} \left(x\dot{x} + y\dot{y} + z\dot{z}\right)$$

$$\frac{\partial V_r}{\dot{y}} = \frac{y}{\sqrt{x^2+y^2+z^2}} = \frac{y}{R} \tag{B.38}$$

For the z-velocity:

$$\frac{\partial V_r}{\partial \dot{z}} = \frac{1}{\sqrt{x^2+y^2+z^2}} \frac{\partial}{\partial \dot{z}} \left(x\dot{x} + y\dot{y} + z\dot{z}\right)$$

$$\frac{\partial V_r}{\dot{z}} = \frac{z}{\sqrt{x^2+y^2+z^2}} = \frac{z}{R} \tag{B.39}$$

Summarised, the Jacobian of radial velocity with respect to the Cartesian spacecraft state is,

$$J_{V_r}\left(\vec{\mathbb{X}}\right) = \begin{bmatrix} \dfrac{-xy\dot{y} - xz\dot{z} + \dot{x}\left(y^2+z^2\right)}{R^3} \\ \dfrac{-xy\dot{x} - yz\dot{z} + \dot{y}\left(x^2+z^2\right)}{R^3} \\ \dfrac{-zx\dot{x} - zy\dot{y} + \dot{z}\left(x^2+y^2\right)}{R^3} \\ \dfrac{x}{R} \\ \dfrac{y}{R} \\ \dfrac{z}{R} \end{bmatrix}^T \tag{B.40}$$

C

Derivation of the radar equation

The derivation of the radar equation is based on the work of Barton [60]. The energy density E_p of the outgoing pulse, measured at a range R from an isotropic antenna (sends in all spherical directions) is,

$$E_p = \frac{E_t}{4\pi R^2} \tag{C.1}$$

Where E_t is the energy of the transmitted pulse and $4\pi R^2$ is the area for spherical expansions at distance R. For an assumed rectangular pulse of width τ and peak power P_t, $E_p = \tau P_t$. For a transmitting antenna with gain G_t, the energy density on the axis of the beam is increased by that gain:

$$E_p = \frac{E_t G_t}{4\pi R^2} = \frac{P_t \tau G_t}{4\pi R^2} \tag{C.2}$$

After reflection from a target with a radar cross section σ, the energy density E_a of the echo incident on the receiving antenna is:

$$E_a = \frac{E_p \sigma}{4\pi R^2} = \frac{P_t \tau G_t \sigma}{\left(4\pi R^2\right)^2} \tag{C.3}$$

The radar receiving antenna, with effective aperture A_e captures energy E:

$$E = E_a A_e = \frac{P_t \tau G_t A_e \sigma}{\left(4\pi R^2\right)^2} \tag{C.4}$$

Note, the receiving antenna gain can also be calculated using:

$$G_r = \frac{4\pi A_e}{\lambda^2} \tag{C.5}$$

where λ is the wavelength. The equation turns into:

$$E = \frac{P_t \tau G_t G_r \lambda^2 \sigma}{\left(4\pi\right)^3 R^4} \tag{C.6}$$

So far, no losses along the transmitter-target-receiver path are considered. To allow for such losses, the factor L_i is added to the equation:

$$E = \frac{P_t \tau G_t G_r \lambda^2 \sigma}{\left(4\pi\right)^3 R^4 L_i} \tag{C.7}$$

In radars, the ratio of the received energy, compared to the noise is an insightful variable. The noise spectral density N_0 referred to a received connected directly to the antenna port, is expressed as:

$$N_0 = kT_s, \tag{C.8}$$

where k is Boltzmann's constant (1.38×10^{-23} J/K) and T_s is the system noise temperature. The signal to noise ratio then becomes:

$$SNR = \frac{S}{N} = \frac{E}{N_0} = \frac{P_t \tau G_t G_r \lambda^2 \sigma}{(4\pi)^3 R^4 k T_s L_i} \tag{C.9}$$